

Multilocal Creaseness Based on the Level-Set Extrinsic Curvature

Antonio M. López, David Lloret, Joan Serrat, and Juan J. Villanueva

Computer Vision Center and Departament d'Informàtica, Universitat Autònoma de Barcelona,
Edifici O, 08193 Cerdanyola, Spain
E-mail: antonio@cvc.uab.es

Received December 11, 1998; accepted October 11, 1999

Creases are a type of ridge/valley structures of an image characterized by local conditions. As creases tend to be at the center of anisotropic grey-level shapes, creaseness can be considered a measure of medialness, and therefore as useful in many image analysis problems. Among the several possibilities, *a priori* the creaseness based on the level-set extrinsic curvature (LSEC) is especially interesting due to its invariance properties. However, in practice, it produces a discontinuous response with a badly dynamic range. The same problems arise with other related creaseness measures proposed in the literature. In this paper, we argue that these problems are due to the very local definition of the LSEC. Therefore, rather than designing an *ad hoc* solution, we propose two new multilocal creaseness measures that we will show to be free of discontinuities and to have a meaningful dynamic range of response. Still, these measures are based on the LSEC idea, to preserve its invariance properties. We demonstrate the usefulness of the new creaseness measures in the context of two applications that we are currently developing in the field of 3D medical image analysis, the rigid registration of CT and MR head volumes and the orientation analysis of trabecular bone patterns. © 2000 Academic Press

Key Words: creases; curvature; divergence; structure tensor; trabecular bone; registration.

1. INTRODUCTION

The *ridges* and *valleys* of a gray-level image tend to be at the center of anisotropic objects; therefore, they are useful skeleton-like descriptors of them. Ridges and valleys are dual in the sense that the valleys of an image are the ridges of the inverted image. In the computer vision literature there is a plethora of different characterizations (algorithmic or mathematical definitions) of the intuitive notion of the ridges/valleys of a landscape. In [31] we classified these characterizations as *local*, *multilocal*, or *global*, according to the region of influence induced by them. Definitions falling in the local class are the *Saint-Venant*/

Haralick condition in 2D [7, 21, 24, 38], generalized to any dimension as *height definition* [10], and the so-called *vertex condition* in 2D [17, 24, 25, 53], generalized to any dimension as *level definition* [10]. From now on, we will use the term *crease* to refer to both ridges and valleys of the local class. We included in the multilocal class the algorithms that extract the *drainage patterns* from digital elevation models by simulating the flow of water over the Earth's surface [35, 44, 49, 16, 12, 50, 8]. Finally, we classified in the global class those algorithms that divide the image domain into districts by special lines called *separatrices* [4, 36, 39, 20, 47, 19], among them the popular *watersheds* [54, 2, 40].

In image analysis, the different characterizations of ridges/valleys can be evaluated on their own merits with regard to their usefulness in different types of applications such as segmentation, drainage pattern delineation, or extraction of medial axes. In this paper we are interested in the last case, that is, in the use of ridges/valleys as an approximation of the center of anisotropic objects in gray-level images. As we argue in [31], the most suitable definitions to extract such medial structures give rise to crease operators. In fact, they are the mostly used in the literature to extract medial structures, as in fingerprint analysis [34, 23], character recognition [55, 26], registration of medical images [11, 33, 53], and computation of medial axes of other gray-level objects [6, 17, 38, 45].

Due to their invariance properties, crease definitions based on *level-set curvatures* are expected to be very useful in many applications. In addition, a one-to-one relationship has been shown between these creases and shape descriptors based on axes of symmetry, both in 2D and 3D [17, 58, 27]. Given a function $L : \Omega \subset \mathbb{R}^d \rightarrow \mathbb{R}$, we define the *level set* associated to a constant l as the set of points $S_l = \{\mathbf{x} \in \Omega \mid L(\mathbf{x}) = l\}$. The continuous variation of l produces all the level sets of L . The simplest situation occurs in 2D ($d = 2$), where L induces a graphic surface which can be thought of as a topographic relief, the level sets being its level curves, like those drawn in a cartographic map and labeled by a height value. Analogously, in 3D we have level surfaces. Each S_l is, in general, composed by several disconnected subsets which can be defined as $(d - 1)$ -dimensional hypersurfaces on Ω . Each $\mathbf{x} \in \Omega$ belongs just to one of these hypersurfaces, defined implicitly by $F(\mathbf{y}) = L(\mathbf{y}) - L(\mathbf{x}) = 0$. The curvatures of these level-set hypersurfaces are invariant under rotations, translations, and uniform scalings, as well as to arbitrary monotonic gray-level transforms [15, 10]. These properties are inherited by the creases based on extrema of the curvatures of the level-set hypersurfaces, that is, the creases characterized by the above-mentioned level definition.

In order to develop the level definition and for its use in the rest of the paper, let us introduce some notation. We define a discrete image as the sampling of a d -dimensional continuous function $L : \Omega \subset \mathbb{R}^d \rightarrow \Gamma \subset \mathbb{R}$. We will consider its partial derivatives up to order n , i.e., the so-called *local jet* of order n , $J_n[L] = \{\partial^j L / \partial \alpha_1 \cdots \partial \alpha_j\}_{j=0}^n$ ($j = 0$ gives L), where $\forall k \in \mathcal{I}_j : \alpha_k \in \mathcal{X}_d$, for \mathcal{I}_j being the set of integers running on $[1, \dots, j]$ and \mathcal{X}_d being the d -dimensional (local) coordinate system $\{x^1, \dots, x^d\}$. We also define the operators $\nabla = (\partial/\partial x^1, \dots, \partial/\partial x^d)$ and $\nabla \nabla = (\nabla^t \cdot \nabla)$ (t means transpose and “ \cdot ” stands for the matrix product), which allow us to define the gradient and the Hessian of a function, respectively. Then, we can define the first-order derivative of L along the direction given by the vector $\mathbf{v} = (v^1, \dots, v^d)^t$ in \mathcal{X}_d coordinates as $L_{\mathbf{v}} = \nabla L \cdot (\mathbf{v}/\|\mathbf{v}\|)$ and the first-order derivative of $L_{\mathbf{v}}$ along the direction given by the vector $\mathbf{w} = (w^1, \dots, w^d)^t$ (second-order derivative of L along \mathbf{v} and \mathbf{w}) as $L_{\mathbf{vw}} = (\mathbf{v}^t/\|\mathbf{v}\|) \cdot \nabla \nabla L \cdot (\mathbf{w}/\|\mathbf{w}\|)$. If we take derivatives of L along the axis of coordinates x^i , we use usual notation L_{x^i} ; that is, in general $L_{\alpha_1 \dots \alpha_j} = \partial^j L / \partial \alpha_1 \cdots \partial \alpha_j$. Finally, x, y, z and i, j, k will denote the continuous and discrete Cartesian coordinates, respectively.

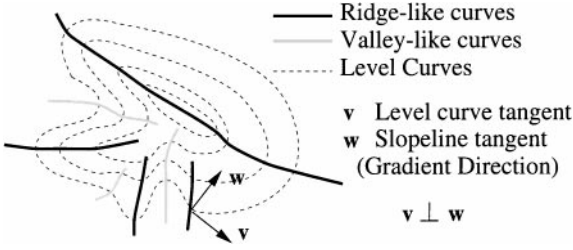


FIG. 1. In 2D crease lines of a certain type are characterized as the loci of extrema of the level-curve curvature κ : negative minima, level-by-level, form valley-like curves and positive maxima form ridge-like ones.

Now we can introduce the level definition of creases as follows. Let $|\xi_1| \geq \dots \geq |\xi_d|$ be the *principal curvatures* of the level hypersurface passing through \mathbf{x} , with $\mathbf{t}_1, \dots, \mathbf{t}_d$ being their corresponding *principal directions* [9, 10]. Then, \mathbf{x} is an m -dimensional crease point if (adapted from [10])

$$\forall i \in \mathcal{I}_{d-m} \quad \nabla \xi_i \cdot \mathbf{t}_i = 0 \quad \text{and} \quad \begin{cases} \mathbf{t}_i^t \cdot \nabla \nabla \xi_i \cdot \mathbf{t}_i < 0 \text{ and } \xi_i > 0 & \text{if ridge} \\ \mathbf{t}_i^t \cdot \nabla \nabla \xi_i \cdot \mathbf{t}_i > 0 \text{ and } \xi_i < 0 & \text{if valley.} \end{cases} \quad (1)$$

Accordingly, in 2D negative minima of the *level-curve curvature*, level by level, form valley-like curves and positive maxima ridge-like curves (Fig. 1), as is also stated in [17, 25, 53]. In 3D we have level surfaces and the crease criterion is based on their principal curvatures.

Unfortunately, the direct computation of extremality criteria such as (1) involves up to fourth-order image derivatives combined into a complex expression (see p. 637 in [17], for the 2D case, and p. 176 in [37], for 3D). Moreover, in practice, the extremality criterion tends to give many irrelevant creases [10, 31] so that an elaborate pruning process may be required. However, most of the time a curvature measure of the level sets yields a sufficiently high value along the center of elongated structures to circumvent the computational drawback by just looking at that curvature as a *creaseness* (ridgeness and valleyiness) measure and then performing a threshold. This is by no means an infrequent situation, but it is precisely for these anisotropic structures that creases are employed as medial descriptors. For example, in 2D the level-curve curvature κ , has been already proposed as a creaseness measure and has been used in the context of medical image analysis [14, 52, 11, 33]. In practice, this approach also removes to a certain extent many of the irrelevant responses given by the strict application of the extremality criterion (1) in 2D. The 3D analogy to the level-curve curvature is the *mean curvature* of the level surfaces κ_M , which is a differential geometric *extrinsic* quantity [9]. Because of that, in the d -dimensional case we use the term *level-set extrinsic curvature* (LSEC), κ_d , for the generalization of κ and κ_M .

At this point we argue that the LSEC should be a good choice as a creaseness measure, that is, as a reliable approximation of *medialness* (minimum distance from a point inside an object to its boundary), not in the sense of providing an actual distance but in the sense of decreasing from the center of an object to its boundary. Of course, other choices are also possible, like the largest principal curvature in absolute value [37, 53]. However, since the LSEC is an average of the principal curvatures, we expect it to be more robust to noise. Moreover, at very anisotropic zones some of the principal curvatures are larger in absolute value than the others. Therefore, they will predominate in the averaging of

principal curvatures, and then the LSEC will capture the most relevant creaseness of the zone. However, through the day-to-day use of the LSEC we can see that there appear two relevant problems, namely, the lack of both *homogeneity* and *continuity* in its response, which prevents the LSEC from being employed as a good medialness approximation.

Accordingly, we devote Section 2 to illustrating the above-mentioned problems and commenting on their implications. In Section 3 we propose an alternative operator to overcome them. The new operator works for d -dimensional images and is termed *multilocal level-set extrinsic curvature* (MLSEC). In the same section, we go a step further and propose a technique which enhances the MLSEC response through the *structure tensor* analysis. In this way, we define a new operator, which we refer to as MLSEC-ST. The next two sections demonstrate the usefulness of the new creaseness measures in two real applications on which we are currently working in the field of 3D medical image analysis, the rigid registration of CT and MR head volumes (Section 4) and the analysis of the dominant orientations of trabecular bone patterns imaged by a CT scanner (Section 5). Finally, Section 6 summarizes the main conclusions. As properly suggested by the reviewers of this paper, we have also included Appendices A and B to clarify some relevant formulas in Section 3.

2. LSEC AS A CREASENESS MEASURE

Besides the invariance properties of LSEC, we must ensure that it achieves other desirable properties in order to be really useful as creaseness measure:

- *Good contrast*. Along an underlying crease the creaseness measure should have a much higher value than along the sections across.
- *Continuity*. The creaseness measure has to be locally high along the whole underlying crease and without gaps since a discontinuous center makes no sense if the object is not discontinuous.
- *Homogeneity*. Along a perceptually homogeneous underlying crease (e.g., a vessel in an MRA, the skull in a CT or an MRI, a road in an aerial image), the creaseness measure should take similar values. A way of pursuing homogeneity consists of ensuring that the creaseness takes values in a well-known dynamic range, in a meaningful way.

The lack of any of such properties reduces the usefulness of a creaseness measure when used as an approximation of medialness and if it is thresholded to obtain creases. Unfortunately, as we are going to see, the LSEC fails to be a continuous and homogeneous measure.

2.1. LSEC Based on the Image Scalar Field

The LSEC can be expressed in terms of the derivatives of L according to tensorial calculus as (see [52], p. 98, and [14], p. 337)

$$\kappa_d = (L_\alpha L_\beta L_{\alpha\beta} - L_\alpha L_\alpha L_{\beta\beta})(L_\gamma L_\gamma)^{-\frac{3}{2}}, \quad \alpha, \beta, \gamma \in \mathcal{X}_d, \quad (2)$$

where the Einstein summation convention must be used to expand this expression for a particular dimension d . The sign of κ_d classifies L as convex ($\kappa_d > 0$) or concave ($\kappa_d < 0$) with respect to the vertical (gray-level) axis, that is, as ridge-like or valley-like, respectively.

For $d = 2$ and using Cartesian coordinates, we obtain the level-curve curvature,

$$\kappa = \kappa_2 = (2L_x L_y L_{xy} - L_y^2 L_{xx} - L_x^2 L_{yy})(L_x^2 + L_y^2)^{-\frac{3}{2}}, \quad (3)$$

and for $d = 3$, we obtain two times the mean curvature of the level surfaces:

$$\begin{aligned} \kappa_M = \frac{1}{2}\kappa_3 = \frac{1}{2} & (2(L_x L_y L_{xy} + L_x L_z L_{xz} + L_y L_z L_{yz}) - L_x^2(L_{yy} + L_{zz}) \\ & - L_y^2(L_{xx} + L_{zz}) - L_z^2(L_{xx} + L_{yy})) (L_x^2 + L_y^2 + L_z^2)^{-\frac{3}{2}}. \end{aligned} \quad (4)$$

In [53] it is shown how κ (p. 193) can be derived by applying the implicit function theorem to the level curves and how κ_M (p. 195) can be derived from the differential geometry of the level surfaces. Appendix A shows how κ and κ_M can be obtained as the particular 2D and 3D cases, respectively, of Eq. (2).

The use of κ as a 2D creaseness measure was already proposed in [14, 52, 11, 33], where the family of operators $L_{\mathbf{v}\mathbf{v}}L_{\mathbf{w}}^\alpha$, $\alpha \in [-1, 0]$, was defined. Taking into account the relation

$$\kappa = -L_{\mathbf{v}\mathbf{v}}/L_{\mathbf{w}}, \quad (5)$$

where $\mathbf{w} = (L_x, L_y)^\dagger$ is the gradient vector and $\mathbf{v} = (L_y, -L_x)^\dagger$ is the tangent to the level curves; $L_{\mathbf{v}\mathbf{v}}$ can be considered as the measure κ weighted by $L_{\mathbf{w}}$ (gradient magnitude) in order to nullify its response at isotropic regions. However, this is a trade-off since $L_{\mathbf{w}}$ is lower inside a ridge/valley region than on its boundary. Thus, we can think of α as a parameter that controls that trade-off.

In [11, 33] the same authors generalized the $L_{\mathbf{v}\mathbf{v}}$ and κ operators to 3D, not by their direct tensorial extension but by means of two new operators that they called $L_{\mathbf{p}\mathbf{p}}$ (ridgeness measure if $L_{\mathbf{p}\mathbf{p}} < 0$) and $L_{\mathbf{q}\mathbf{q}}$ (valleyiness measure if $L_{\mathbf{q}\mathbf{q}} > 0$), where \mathbf{p} and \mathbf{q} are the principal directions of the level surfaces. Similarly to the 2D case, the families of operators $L_{\mathbf{p}\mathbf{p}}L_{\mathbf{w}}^\alpha$ and $L_{\mathbf{q}\mathbf{q}}L_{\mathbf{w}}^\alpha$ were defined. In Section 4 we will compare $L_{\mathbf{p}\mathbf{p}}$ and $L_{\mathbf{q}\mathbf{q}}$ to the new operators we propose.

2.2. Problems of the LSEC as a Creaseness Measure

Even though in theory the LSEC is a good creaseness measure, we have found that its output is not sufficiently satisfactory since it contains discontinuities at places where we would not expect any reduction of creaseness because they are at the center of elongated objects. Moreover, the LSEC can have an extremely large dynamic range but can have only a few points with values at the upper and lower bounds, which we call *outliers*. This makes creaseness differ from medialness since these outliers are not “more in the center” than other points with a high, but not outlier, creaseness value.

A 2D example can be seen in Fig. 2, where we want to obtain a measure which is high along the center of the skull from a CT and an MR slice, and low elsewhere. We observe that discontinuities are frequent along these centers. Notice that gaps cannot be locally distinguished from points that actually must have low creaseness. This affects the use of the creaseness measure itself and the extraction of creases by thresholding it since *crease finders* should have to decide heuristically which direction to follow when they reach such discontinuities. Moreover, the results in Fig. 2 are shown for after the application of the following gray-level transform for a given $l > 0$:

$$T(I(\mathbf{x}), l) = \begin{cases} l & \text{if } I(\mathbf{x}) > l \\ -l & \text{if } I(\mathbf{x}) < -l \\ I(\mathbf{x}) & \text{otherwise.} \end{cases} \quad (6)$$

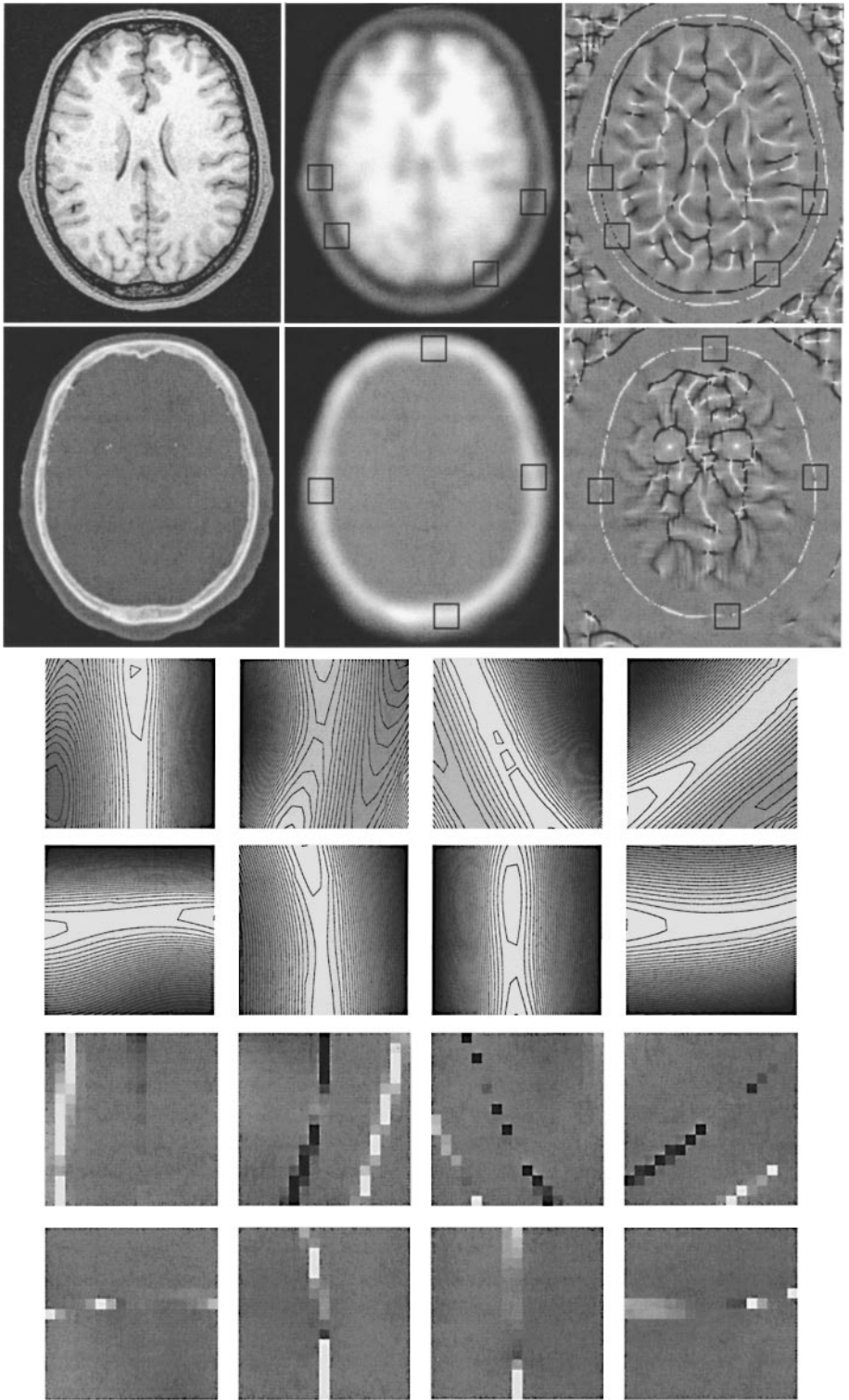


FIG. 2. First row, from left to right: (a) MR slice. (b) Smoothed with a Gaussian kernel. (c) $T(\kappa, 1.0)$ of the smoothed image. Second row: (d) CT slice. (e) Smoothed. (f) $T(\kappa, 1.0)$. Third row: (g) Level curves from the ROIs of the smoothed MR slice (in this case, with an inverted gray scale for the sake of visualization). Fourth row: (h) The same as for the CT. Fifth row: (i) Zoom of the ROIs of κ computed from the MR slice. Sixth row: (j) The same as for the CT.

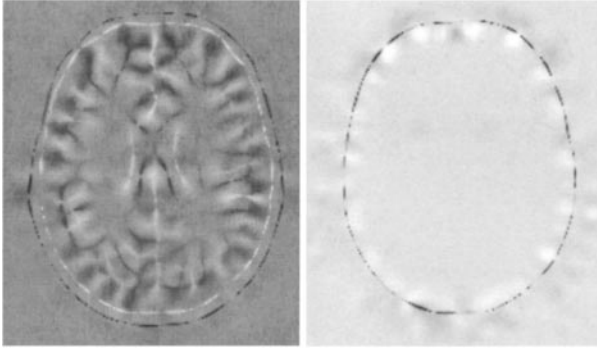


FIG. 3. Left: (a) L_{vv} from the smoothed MR slice in Fig. 2b. Right: (b) The same as from the smoothed CT slice in Fig. 2e. In both cases L_{vv} was computed according to its expression in terms of image derivatives, not by computing κ and L_w and then using Eq. (5).

The purpose of this transform is to select a suitable interval of the LSEC response before doing the usual 8-bits contrast maximization, for the sake of visualization. Without applying T to the LSEC response we would only see its outlier values.

The measure L_{vv} improves the previous results because it has a more homogeneous dynamic range and removes the background response, but still it presents many discontinuities along the center of elongated gray-level objects (Fig. 3). In 3D, operators such as κ_M , L_{pp} , and L_{qq} exhibit analogous problems, as we will see in Section 4.

3. MLSEC AS A CREAENESS MEASURE

If we think for a moment of an image as a continuous function, we can see that by traveling along the center of elongated structures contained in it we go up and down, passing through generic critical points (maxima, minima, and saddle points), that is, points where $L_w = 0$ but $\det(\nabla\nabla L) \neq 0$. From Eq. (2) we know that the LSEC is ill-defined at such points since the gradient magnitude $L_w = (L_\gamma L_\gamma)^{1/2}$ vanishes. In 2D, for instance, we could appeal to the

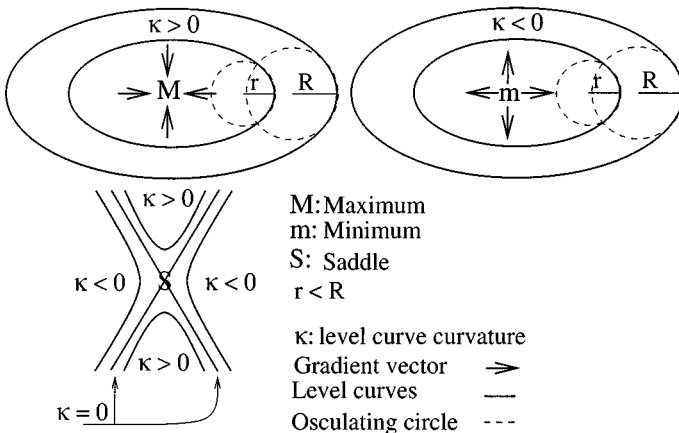


FIG. 4. Scheme of the level curves around generic critical points. Around extrema the radius of curvature of the level curves goes to zero; therefore its inverse, κ , goes to $+\infty$ at maxima and to $-\infty$ at minima. A saddle point is the intersection of two straight segments of level curve. Thus, we can consider that at a saddle point κ vanishes.

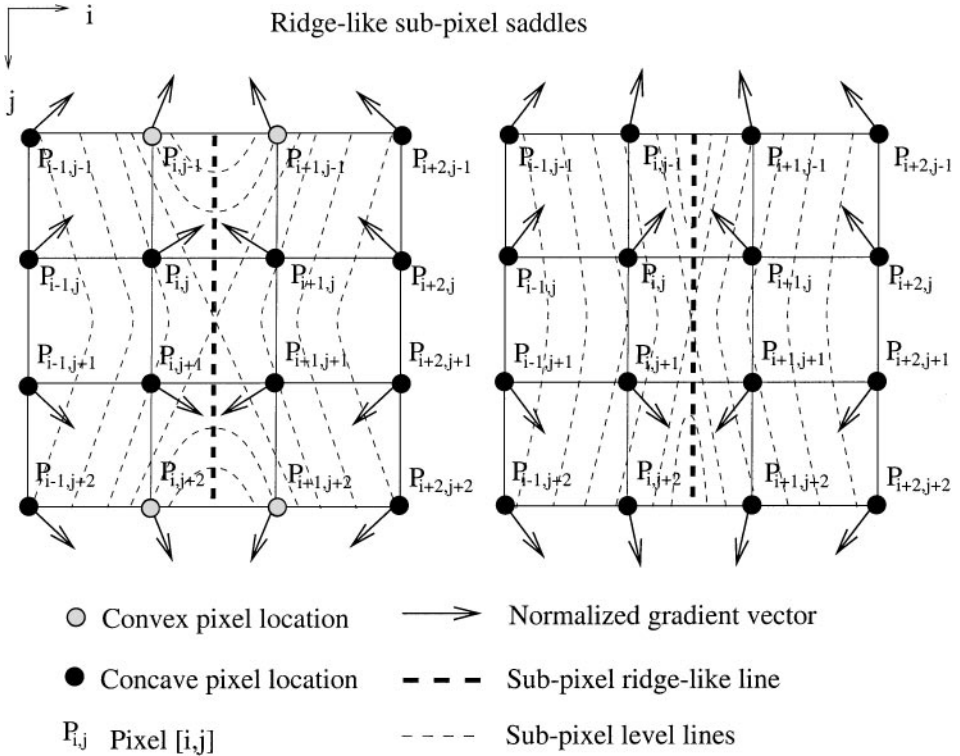


FIG. 5. Sampling around a saddle point. Discrete convex paths (ridge-like) are broken due to the sampling, mostly at the surrounding concave area. The more elongated the saddle, the longer the interruption.

geometry of the level curves around the critical points (Fig. 4) to assign a “coherent” value to κ . At a saddle the curvature of the level curves vanishes, at a maximum it has a value of $+\infty$, and at a minimum it has a value of $-\infty$, but this precisely would make κ discontinuous and inhomogeneous if critical points are placed along the center of an anisotropic object.

On the other hand, in the discrete domain it is quite unlikely to find a pixel where $L_w = 0$, except in a flat area. The actual critical points are placed at sub-pixel coordinates. However, it is precisely in the discrete domain where the problems of the LSEC measure arise, mainly around saddle points where even a *change of sign barrier* occurs. Figure 5 shows a scheme of the sampling of a 2D ridge-like saddle-placed sub-pixel, which is reached by a ridge-like curve. Notice how the underlying surface is mainly sampled at concave zones ($\kappa < 0$) in such a way that, by discretizing κ , ridgeness ($\kappa > 0$) is interrupted by valleyiness ($\kappa < 0$). This is true even if we sample the analytic expression of κ ; that is, it is not a problem of how we discretize Eq. (3). Moreover, intuitively it is clear that the more ridge-like the saddle is, the larger the interruption is. This is the case for the selected ROIs of the center of the skull from the smoothed MR and CT slices of Fig. 2. We see that the discontinuities of κ and L_{vv} along the skull do not correspond to any relevant break of that anatomical structure in the smoothed slices. In addition, saddles are more elongated when the variation of gray-levels along the underlying crease is very gentle, which is the usual situation, mainly if we are processing images of the linear scale-space stack [52, 14].

In this paper we argue that these problems are due to the very local definition of the LSEC, which is not appropriate for the discrete domain, that is, for real-life image analysis.

Therefore, we devote Section 3.1 to defining a multilocal operator based on the LSEC, the MLSEC, which will be shown to overcome the problem of discontinuities around critical points and the inhomogeneity of the LSEC response. In Section 3.2 we will also present a natural improvement of this operator, the MLSEC-ST operator, by borrowing ideas from the analysis of oriented textures. In Section 3.3 we provide some comments on the computational aspects of these operators.

3.1. LSEC Based on the Image Gradient Vector Field

In 2D, κ can be defined through its geometric relationship with the slope lines, which are the lines integrating the gradient vector field \mathbf{w} and are, therefore, orthogonal to the level curves. Due to the orthogonality, when level curves are parallel straight lines, slope lines are also parallel and straight, and when the level curves bend, the slope lines diverge/converge (Fig. 6). Therefore, it is clear that there is a connection between the curvature of the level curves and the degree of parallelism of the slope lines. In vector calculus we have the divergence operator which measures this degree of parallelism. The divergence of a d -dimensional vector field $\mathbf{u}: \mathbb{R}^d \rightarrow \mathbb{R}^d$, $\mathbf{u}(\mathbf{x}) = (u^1(\mathbf{x}), \dots, u^d(\mathbf{x}))^t$ is defined as [48]

$$\text{div}(\mathbf{u}) = \sum_{i=1}^d \frac{\partial u^i}{\partial x^i}. \tag{7}$$

Now, if we denote by $\mathbf{0}_d$ the d -dimensional zero vector, we can define $\bar{\mathbf{w}}$, the normalized gradient vector field of $L: \mathbb{R}^d \rightarrow \mathbb{R}$, as

$$\bar{\mathbf{w}} = \begin{cases} \mathbf{w}/\|\mathbf{w}\| & \text{if } \|\mathbf{w}\| > 0 \\ \mathbf{0}_d & \text{if } \|\mathbf{w}\| = 0, \end{cases} \tag{8}$$

and then it can be shown (Appendix B) that

$$\kappa_d = -\text{div}(\bar{\mathbf{w}}). \tag{9}$$

Equation (9) allows for a new geometric interpretation of κ_d . To fix ideas let us return to the 2D case, and let \mathbf{x} be a point where the divergence of a 2D vector field \mathbf{u} has to be computed. Let \mathcal{C} be a simple closed curve in \mathbb{R}^2 parameterized by ℓ , which encloses the point \mathbf{x} ; let \mathbf{n} be its unitary normal vector and ω the area enclosed by \mathcal{C} . Figure 7 depicts the situation. Then the divergence of \mathbf{u} at \mathbf{x} can also be defined as [48]

$$\text{div}(\mathbf{u}) = \lim_{\omega \rightarrow 0} \frac{1}{\omega} \int_{\mathcal{C}} \mathbf{u}^t \cdot \mathbf{n} \, d\ell. \tag{10}$$

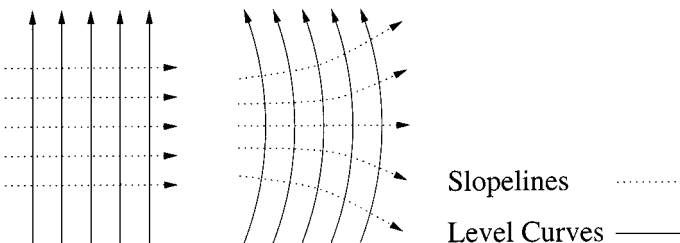


FIG. 6. Slope lines diverge/converge according to the curvature of the level curves.

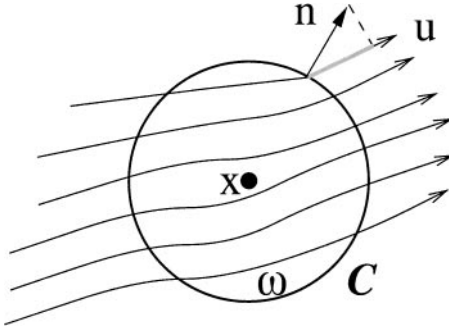


FIG. 7. Geometry involved in the definition of the divergence of a vector field \mathbf{u} at \mathbf{x} .

For any dimension d , we can generalize this definition by assuming that \mathcal{C} is a $(d - 1)$ -dimensional simple closed boundary of a neighborhood \mathcal{W} ($\partial\mathcal{W} = \mathcal{C}$) of volume ω including \mathbf{x} and that $d\ell$ is the $(d - 1)$ -dimensional volume element of \mathcal{C} (e.g., if \mathcal{C} is a closed surface then $d\ell$ is an area element).

Taking the limit in Eq. (10) for $\mathbf{u} = \bar{\mathbf{w}}$ makes Eq. (9) hold in the continuous domain. However, we argue that it is precisely the infinitesimal process which gives rise to the problems of the LSEC as a creaseness measure. Therefore, we propose in this paper the substitution of the local definition of κ_d by a multilocal definition based on a discretized version of Eq. (10), where the multilocality is achieved by assuming that the neighborhood \mathcal{W} or, analogously, its boundary \mathcal{C} , is a selectable parameter. That is, to compute $\text{div}(\bar{\mathbf{w}})$ at \mathbf{x} we will take into account gradient vectors along the path \mathcal{C} around \mathbf{x} . The rationale of our proposal is to try to capture the tendency to diverge or converge of a vector field in a neighborhood of finite size rather than computing the infinitesimal tendency of the vector field. We believe that this is more in agreement with our perception of the crease structures.

According to this reasoning, for a given dimension d we will denote $\bar{\kappa}_d$ the multilocal level-set extrinsic curvature (MLSEC) based on Eqs. (8), (9), and (10), given a selected \mathcal{C} . This can be stated through the following definitions.

DEFINITION 1 (divergence for regular grids). In the d dimensional Euclidean space, let $\mathcal{B} = \{\mathbf{i}_1, \dots, \mathbf{i}_r\}$ represent the set of d -xels that form the discrete boundary \mathcal{C} of a given neighborhood or window \mathcal{W} ($\mathcal{C} = \partial\mathcal{W}$) centered at a d -xel \mathbf{i} , and let $\mathcal{U} = \{\mathbf{u}_1, \dots, \mathbf{u}_r\}$, where $\forall k \in \mathcal{I}_r: \mathbf{u}_k = \mathbf{u}(\mathbf{i}_k)$ for a d -dimensional vector field \mathbf{u} . Then, according to Eq. (10), the divergence of \mathbf{u} at \mathbf{i} can be discretized as

$$\text{div}(\mathbf{u}) = \frac{\delta\ell}{\omega} \sum_{k=1}^r \mathbf{u}_k^t \cdot \mathbf{n}_k, \quad (11)$$

ω being the volume of \mathcal{W} , $\mathcal{N} = \{\mathbf{n}_1, \dots, \mathbf{n}_r\}$ the unit normal vectors to \mathcal{C} at each boundary site, that is, $\forall k \in \mathcal{I}_r: \mathbf{n}_k = \mathbf{n}(\mathbf{i}_k)$, and $\delta\ell$ the discrete volume element of \mathcal{C} that we assume to be constant. From now on, we will refer to r as adjacency.

Given a vector field, in this paper we assume the use of the same window \mathcal{W} to compute its divergence at any point; therefore, $\delta\ell$ and ω are constant. This means that we can remove the scaling factor $\delta\ell/\omega$ when computing $\bar{\kappa}_d$ since it would be just a global scaling of the creaseness measure. Therefore, we redefine the discrete divergence as follows.

DEFINITION 2 (scaled divergence for regular grids). Under the conditions of Definition 1, we redefine the divergence of \mathbf{u} at \mathbf{i} as

$$\operatorname{div}(\mathbf{u}) = \frac{d}{r} \sum_{k=1}^r \mathbf{u}_k^t \cdot \mathbf{n}_k. \quad (12)$$

Here we have introduced the scaling factor d/r for a better geometric interpretation of the dynamic range of $\bar{\kappa}_d$ as we will explain shortly.

DEFINITION 3 (MLSEC). According to the divergence operator in Eq. (12), we define our MLSEC operator for a discrete domain as

$$\bar{\kappa}_d = -\operatorname{div}(\bar{\mathbf{w}}) = -\frac{d}{r} \sum_{k=1}^r \bar{\mathbf{w}}_k^t \cdot \mathbf{n}_k, \quad (13)$$

where the adjacency r will be given by the specific \mathcal{C} we use.

The simplest case holds in 2D ($d=2$) with \mathcal{B} composed by the four nearest neighbors of each pixel ($r=4$). That is, for the pixel $P_{i,j}$ of coordinates $[i, j]$, we have $\mathcal{B} = \{P_{i,j-1}, P_{i+1,j}, P_{i,j+1}, P_{i-1,j}\}$ and $\mathcal{N} = \{\mathbf{n}_N, \mathbf{n}_E, \mathbf{n}_S, \mathbf{n}_W\}$, according to the scheme of Fig. 8a. Therefore, the 2D MLSEC at $P_{i,j}$ is computed as

$$\begin{aligned} \bar{\kappa}_2[i, j] &= -\frac{2}{4}(\bar{\mathbf{w}}^t[i, j-1] \cdot \mathbf{n}_N + \bar{\mathbf{w}}^t[i+1, j] \cdot \mathbf{n}_E \\ &\quad + \bar{\mathbf{w}}^t[i, j+1] \cdot \mathbf{n}_S + \bar{\mathbf{w}}^t[i-1, j] \cdot \mathbf{n}_W) \\ &= -\frac{1}{2}(\bar{w}^1[i+1, j] - \bar{w}^1[i-1, j] + \bar{w}^2[i, j+1] - \bar{w}^2[i, j-1]), \end{aligned} \quad (14)$$

where \bar{w}^1 and \bar{w}^2 are the components of $\bar{\mathbf{w}}$ in 2D. From now on, we will denote this 2D MLSEC operator $\bar{\kappa}^\diamond$, where the symbol \diamond recalls the shape of \mathcal{C} .

The 3D equivalent ($d=3$) consists of taking \mathcal{B} as the neighbors of a voxel given by the 6-adjacency ($r=6$). That is, $\mathcal{B} = \{P_{i,j-1,k}, P_{i+1,j,k}, P_{i,j+1,k}, P_{i-1,j,k}, P_{i,j,k-1}, P_{i,j,k+1}\}$ for the voxel $P_{i,j,k}$ and $\mathcal{N} = \{\mathbf{n}_N, \mathbf{n}_E, \mathbf{n}_S, \mathbf{n}_W, \mathbf{n}_F, \mathbf{n}_B\}$, according to the scheme of Fig. 8b. Thus, in this case the 3D MLSEC at $P_{i,j,k}$ is computed as

$$\begin{aligned} \bar{\kappa}_3[i, j, k] &= -\frac{1}{2}(\bar{w}^1[i+1, j, k] - \bar{w}^1[i-1, j, k] + \bar{w}^2[i, j+1, k] \\ &\quad - \bar{w}^2[i, j-1, k] + \bar{w}^3[i, j, k+1] - \bar{w}^3[i, j, k-1]), \end{aligned} \quad (15)$$

where \bar{w}^1 , \bar{w}^2 , and \bar{w}^3 are the components of $\bar{\mathbf{w}}$ in 3D. From now on, we will denote this 3D MLSEC operator $\bar{\kappa}_M^\diamond$ ($\bar{\kappa}_M^\diamond/2$ is a “substitute” for κ_M).

We can generalize these specific operators to any dimension d as $\bar{\kappa}_d^\diamond$. In this case we have $r=2d$ ($2d$ -adjacency), and it is easy to show [30] that

$$\bar{\kappa}_d^\diamond = -\frac{1}{2} \sum_{k=1}^d \bar{w}^k[i^1, \dots, i^k+1, \dots, i^d] - \bar{w}^k[i^1, \dots, i^k-1, \dots, i^d]. \quad (16)$$

Notice that Eq. (16) is a sum of first-order centered finite differences (CFDs) as defined in Table I. This means that the boundary based on the $2d$ -adjacency, which delimits the

TABLE I
Approximation of the First- and Second-order Partial Derivatives
of $L[i, j]$ Using CFDs

$\delta_x L[i, j]$	$(L[i + 1, j] - L[i - 1, j])/2$
$\delta_y L[i, j]$	$(L[i, j + 1] - L[i, j - 1])/2$
$\delta_{xx} L[i, j]$	$(L[i + 2, j] - 2L[i, j] + L[i - 2, j])/4$
$\delta_{yy} L[i, j]$	$(L[i, j + 2] - 2L[i, j] + L[i, j - 2])/4$
$\delta_{xy} L[i, j] = \delta_{yx} L[i, j]$	$(L[i + 1, j + 1] + L[i - 1, j - 1] - L[i - 1, j + 1] - L[i + 1, j - 1])/4$

Note. The second-order CFDs are obtained as CFDs of the first-order approximations.

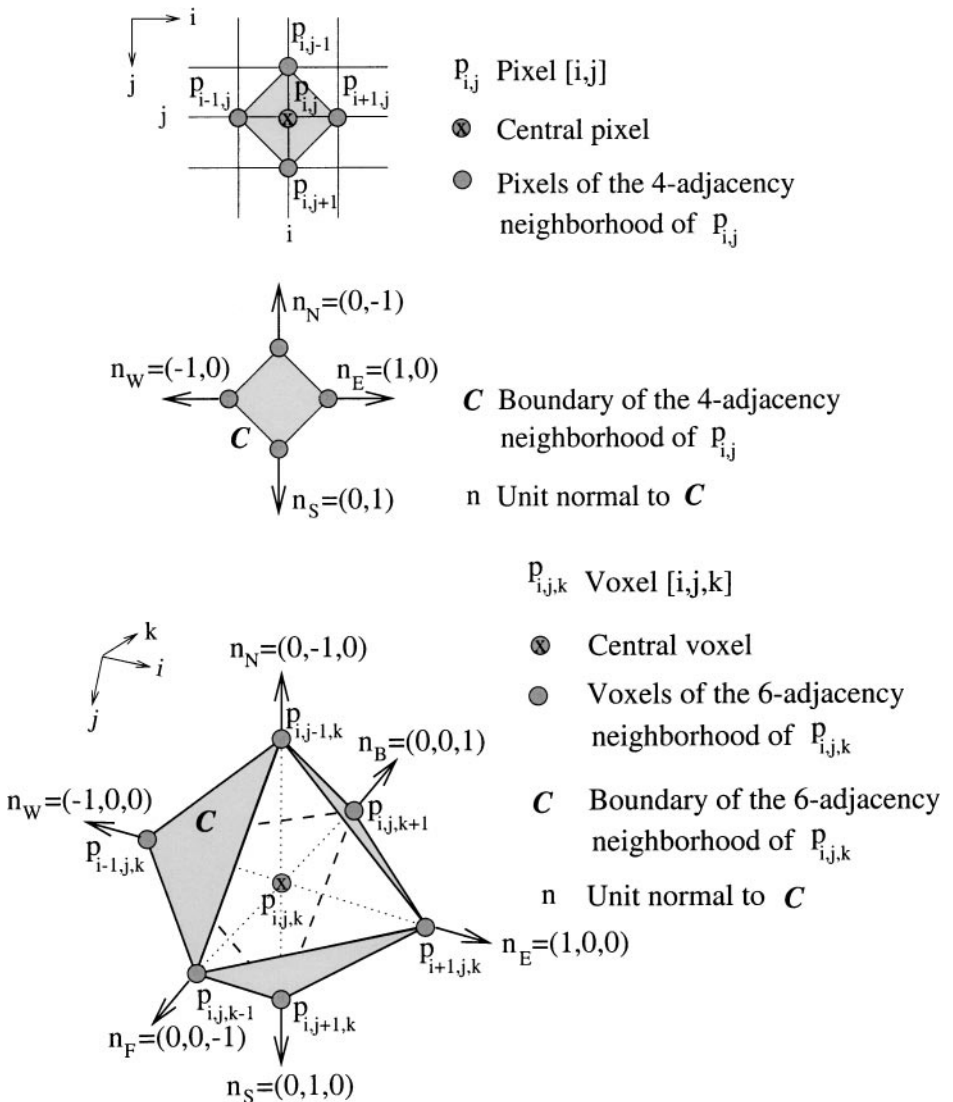


FIG. 8. Top and middle: (a) Boundary C of a rectangular grid neighborhood according to the 4-adjacency in 2D. Bottom: (b) The 3D analogy is the 6-adjacency.

smallest neighborhood we can use in a rectangular grid to discretize the integral form of the divergence (Eq. (12)), provides the same operator as discretizing the differential form of the divergence (Eq. (7)) by using CFDs to approximate the first-order partial derivatives.

Now let us see why $\bar{\kappa}_d$ does not suffer the problems of κ_d . First, we show that it has a well-defined dynamic range according to the following theorem.

THEOREM 1. *According to Eq. (13) we can state that*

$$|\bar{\kappa}_d| \leq d. \quad (17)$$

Proof. Since $\bar{\mathbf{w}}$ is a normalized vector field and each normal \mathbf{n} in \mathcal{B} is also a unitary vector, we have that, at any d -xel,

$$|\bar{\mathbf{w}}^\dagger \cdot \mathbf{n}| = \|\bar{\mathbf{w}}\| \|\mathbf{n}\| |\cos(\text{angle}(\bar{\mathbf{w}}, \mathbf{n}))| \leq 1.$$

Therefore,

$$|\bar{\kappa}_d| = |\text{div}(\bar{\mathbf{w}})| = \frac{d}{r} \left| \sum_{k=1}^r \bar{\mathbf{w}}_k^\dagger \cdot \mathbf{n}_k \right| \leq \frac{d}{r} \left| \sum_{k=1}^r 1 \right| = d.$$

■

Moreover, it can be shown [30] that $|\bar{\kappa}_d|$ approaches the codimension of the crease structures from/to which the gradient vector field diverges/converges. In practice, this means that if we want to extract crease structures of dimension m from a d -dimensional image, $m \leq d$, then, given $0 < \epsilon < 1$, we have to double threshold $\bar{\kappa}_d$ between $\max\{0, (d - m - \epsilon)\}$ and $\min\{(d - m + \epsilon), d\}$, in the case of ridges, and between $\max\{-d, (m - d - \epsilon)\}$ and $\min\{(m - d - \epsilon), 0\}$, for valleys. In fact, along an m -dimensional crease there can be crease points of codimension lower than m . For example, in 2D we can have a ridge line passing through a local maximum, and we do not want to discard it since a gap would be created along that ridge line. A pragmatic decision we have made, which works quite well in practice, consists of using a threshold value selecting the creases of the dimension that we want and also the creases of lower dimension. This means that to extract crease structures of dimension m we have to threshold $\bar{\kappa}_d$ at $\max\{0, (d - m - \epsilon)\}$ for ridges and at $\min\{(m - d - \epsilon), 0\}$ for valleys. In theory, this approach can produce isolated creases of dimension lower than m , but in practice they can be easily removed by looking at criteria such as their area in 2D, volume in 3D, and so on. In fact, in the applications we review in this paper (Sections 4 and 5) no post-processing of any type was needed: the output of our operators was used “as is.” On the other hand, the exact ϵ depends on the adjacency r we use to compute the divergence. However, for a fixed we verified in a number of applications on different kinds of images that a fine tuning is not needed at all.

The formal proof of how the $\bar{\kappa}_d$ operator avoids the discontinuities produced by κ_d demands the introduction of several definitions and intermediate assertions with their corresponding proofs, which can be found in [30]. Instead, for the sake of simplicity, in this paper we merely expose the basic idea which we think will be sufficient to clarify the situation.

In d dimensions, extrema are not a problem at all for the MLSEC. By examining the normalized gradient vector field, we see that maxima are perfect attractors (e.g., Fig. 4), and, therefore, the MLSEC reaches its maximum value d . Analogously, minima are perfect

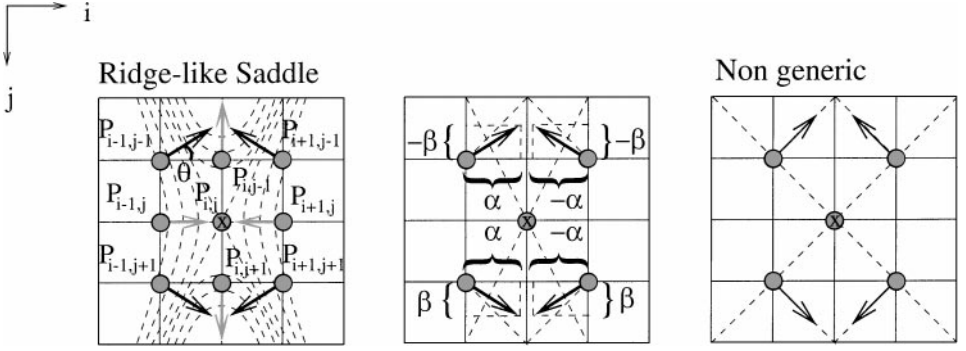


FIG. 9. Normalized gradient vectors around a ridge-like saddle. If we want to compute the divergence of this vector field at the central point, with the 4-adjacency only the vectors in gray are involved and with the 8-adjacency both the gray and black vectors are. The discontinuous gray-level lines are the level curves. The third column shows a nonstable situation, where the divergence based on both the 4-adjacency and the 8-adjacency vanishes. Again, this is an unstable case.

repellers (e.g., Fig. 4), and the MLSEC reaches its minimum value $-d$. Notice that this is in agreement with our previous statements about the codimension of the creases: since the extrema are points, they can be thought of as creases of dimension 0; therefore, their codimension is d . This means that, unlike the LSEC, any MLSEC measure is well-defined at the extrema of the image.

To clarify how the MLSEC allows us to circumvent the problems of change of sign barrier (discontinuities) that the LSEC presents, let us consider the 2D example of Fig. 9. Suppose we compute the creaseness measure $\bar{\kappa}^\diamond$ at the central pixel $P_{i,j}$. According to Fig. 8a we see that in the ridge-like saddle we have $(\bar{\mathbf{w}}^t[i, j-1] \cdot \mathbf{n}_N + \bar{\mathbf{w}}^t[i, j+1] \cdot \mathbf{n}_S) = -(\bar{\mathbf{w}}^t[i-1, j] \cdot \mathbf{n}_W + \bar{\mathbf{w}}^t[i+1, j] \cdot \mathbf{n}_E)$. Therefore, following Eq. (14) we obtain $\bar{\kappa}^\diamond[i, j] = 0$. Notice that this is in agreement with the geometric interpretation of the level-curve curvature at a saddle point. However, we are obtaining a low creaseness at $P_{i,j}$, and we would expect it to be high if these saddles were at the center of an elongated gray-level structure. This means that $\bar{\kappa}^\diamond$ will produce a gap here, although not a change of sign barrier as κ would do, which would be worse. To avoid this we simply increase the neighborhood \mathcal{W} involved in the definition of the divergence operator. Let us change, for instance, to the 8-adjacency as shown in Fig. 10, and let $\bar{\kappa}^\square$ be the corresponding MLSEC measure. In this case we have

$$\begin{aligned} \bar{\kappa}^\square[i, j] = & -\frac{1}{4}(\bar{\mathbf{w}}^t[i, j-1] \cdot \mathbf{n}_N + \bar{\mathbf{w}}^t[i+1, j-1] \cdot \mathbf{n}_{NE} + \bar{\mathbf{w}}^t[i+1, j] \cdot \mathbf{n}_E \\ & + \bar{\mathbf{w}}^t[i+1, j+1] \cdot \mathbf{n}_{ES} + \bar{\mathbf{w}}^t[i, j+1] \cdot \mathbf{n}_S + \bar{\mathbf{w}}^t[i-1, j+1] \cdot \mathbf{n}_{SW} \\ & + \bar{\mathbf{w}}^t[i-1, j] \cdot \mathbf{n}_W + \bar{\mathbf{w}}^t[i-1, j-1] \cdot \mathbf{n}_{WN}), \end{aligned} \quad (18)$$

which expands as

$$\begin{aligned} \bar{\kappa}^\square[i, j] = & \bar{\kappa}^\diamond[i, j]/2 - (\bar{w}^1[i+1, j-1] - \bar{w}^1[i-1, j-1] + \bar{w}^1[i+1, j+1] \\ & - \bar{w}^1[i-1, j+1] + \bar{w}^2[i-1, j+1] - \bar{w}^2[i-1, j-1] \\ & + \bar{w}^2[i+1, j+1] - \bar{w}^2[i+1, j-1])/4\sqrt{2}. \end{aligned} \quad (19)$$

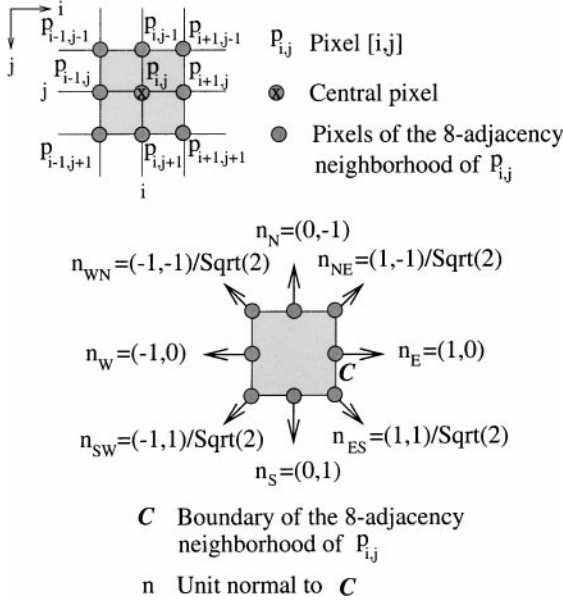


FIG. 10. Boundary C involved in the definition of $\bar{\kappa}_2$ according to the 8-adjacency in 2D that is $\bar{\kappa}^\square$.

We have seen that $\bar{\kappa}^\diamond[i, j] = 0$, and according to Fig. 9 we also have

$$\begin{aligned}
 \bar{w}^1[i + 1, j - 1] &= \bar{w}^1[i + 1, j + 1] = -\alpha \\
 \bar{w}^1[i - 1, j - 1] &= \bar{w}^1[i - 1, j + 1] = \alpha \\
 \bar{w}^2[i - 1, j - 1] &= \bar{w}^2[i + 1, j - 1] = -\beta \\
 \bar{w}^2[i - 1, j + 1] &= \bar{w}^2[i + 1, j + 1] = \beta,
 \end{aligned}$$

for $\alpha = \cos(\theta)$ and $\beta = \sin(\theta)$. Therefore,

$$\bar{\kappa}^\square[i, j] = \frac{1}{\sqrt{2}}(\alpha - \beta).$$

If $\alpha > \beta$ the saddle is ridge-like and $\bar{\kappa}^\square > 0$. Analogously, if $\alpha < \beta$ the saddle is valley-like and $\bar{\kappa}^\square < 0$. The case $\alpha = \beta$, shown also in Fig. 9, consists of an unstable situation. The specific value of $\bar{\kappa}^\square$ can be assessed by noticing that $\alpha^2 + \beta^2 = 1$; therefore,

$$\bar{\kappa}^\square = \frac{1}{\sqrt{2}}(\alpha - \sqrt{1 - \alpha^2}).$$

Figure 11 depicts $\bar{\kappa}^\square$ as a function of θ . This example shows how we can avoid discontinuities at saddle points by increasing the size of the neighborhood.

At a given dimension d , the MLSEC measure based on the $2d$ -adjacency, $\bar{\kappa}_d^\diamond$, vanishes at saddles only if d is even. Otherwise, the value of $\bar{\kappa}_d^\diamond$ will capture the tendency of the gradient vector field to converge or diverge [30]. When d is even we can still capture this tendency by increasing the size of the neighborhood used to compute the divergence, as we have done in the previous 2D example.

On the other hand, we have already mentioned that, in practice, critical points are placed at sub-pixel coordinates. This implies that around a maximum the MLSEC will just have

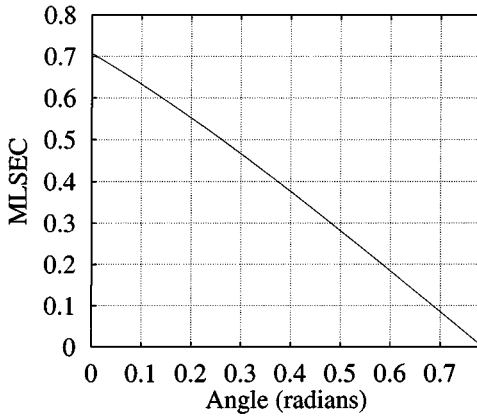


FIG. 11. Plot of the MLSEC measure $\bar{\kappa}^\square$ as a function of the angle $0 \leq \theta \leq (\pi/4)$ given by $\alpha = \cos(\theta)$.

a value near d , and around a minimum near $-d$. In the case of the saddles, the fact that they are usually placed at sub-pixel coordinates implies that just by using $\bar{\kappa}_d^\diamond$ we are already able to detect ridgeness or valleyiness without suffering from discontinuities. For example, in Fig. 5 it is clear that $\bar{\kappa}^\diamond$ will not vanish since the saddle is placed at sub-pixel level: what is captured is the convergence of the normalized gradient vector field.

Figure 12 shows the results of applying the $\bar{\kappa}^\diamond$ operator to the smoothed MR and CT slices of Fig. 2. Since the MLSEC has a well-behaved dynamic range, we show directly the output of $\bar{\kappa}^\diamond$ without using the transform T of Eq. (6). Notice also how the discontinuities along the center of the skull disappear with respect to Fig. 2. Figure 13 shows a similar comparison on a synthetic image having many anisotropic critical points placed at sub-pixel locations.

In summary, we have shown that, unlike the LSEC, the MLSEC yields a continuous and homogeneous response, and both the LSEC and the MLSEC are well-contrasted creaseness measures. In addition, as the MLSEC is based on the relative orientations of the normalized gradient vector field, it is invariant under rigid transforms and scalings of the image axes, and under arbitrary monotonic gray-level transforms. With respect to the thickness of the response, we can state as a general rule that it increases with the neighborhood selected to compute the divergence. Figure 14 illustrates the results of computing $\bar{\kappa}_2$ by varying the radius of a circular neighborhood. In spite of this, it can be an advantage in specific applications like that in Section 5. However, we must be careful when increasing the neighborhood so that close convex/concave regions do not interfere with each other.

3.2. LSEC Based on the Image Structure Tensor Field

Once we have established $\bar{\kappa}_d$ as a good creaseness measure, we can go further and enhance it by modifying, in a convenient way, the gradient vector field of the image before applying the divergence operator. We want to filter the gradient vector field in such a way that the configurations of Fig. 15a approach those of Fig. 15b since then attraction/repulsion, and therefore creaseness, will be higher. At the same time, the qualitative behavior of the gradient vector field at regions where there is neither attraction nor repulsion must remain unchanged. This filtering can be carried out in a natural way through the *structure tensor*, which is a well-known tool for analyzing oriented textures [3, 22]. Moreover, without extra

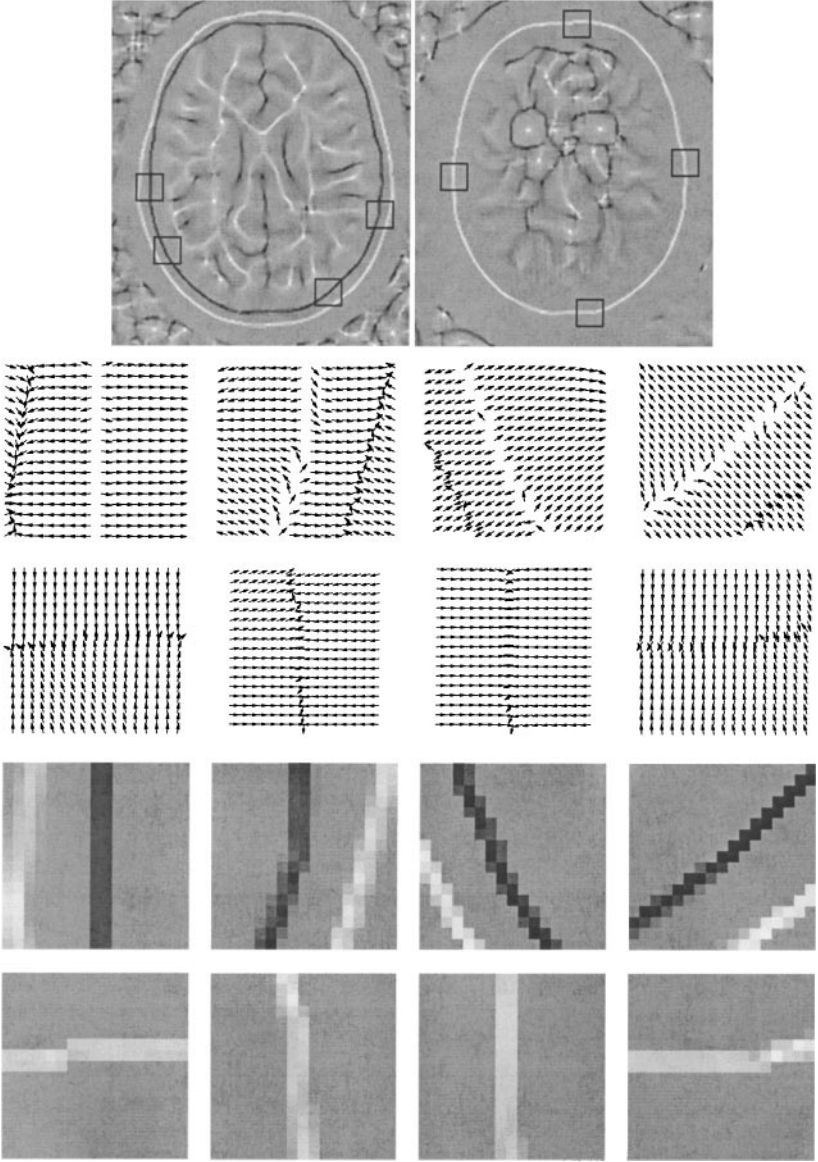


FIG. 12. First row, from left to right: (a) $\bar{\kappa}^\diamond$ of the smoothed MR slice in Fig. 2. (b) The same as for the CT. Second row: (c) Normalized gradient vector field from the ROIs of the smoothed MR slice. Third row: (d) The same as for the CT. Fourth row: (e) $\bar{\kappa}^\diamond$ of the ROIs from the MR slice. Fifth row: (f) The same as for the CT.

computational cost, we get a coarse measure of the degree of anisotropy that will allow us to attenuate the creaseness measure at zones in which we are not interested, like flat regions.

In the d -dimensional space, given a symmetric neighborhood of size σ_1 centered at a given point \mathbf{x} , namely, $\mathcal{N}(\mathbf{x}; \sigma_1)$, the structure tensor is defined to be the symmetric and semi-positive definite $d \times d$ matrix

$$\mathbf{S}(\mathbf{x}; \sigma_1) = \mathcal{N}(\mathbf{x}; \sigma_1) * (\mathbf{w}(\mathbf{x}) \cdot \mathbf{w}^t(\mathbf{x})), \quad (20)$$

where the convolution “ $*$ ” is elementwise.

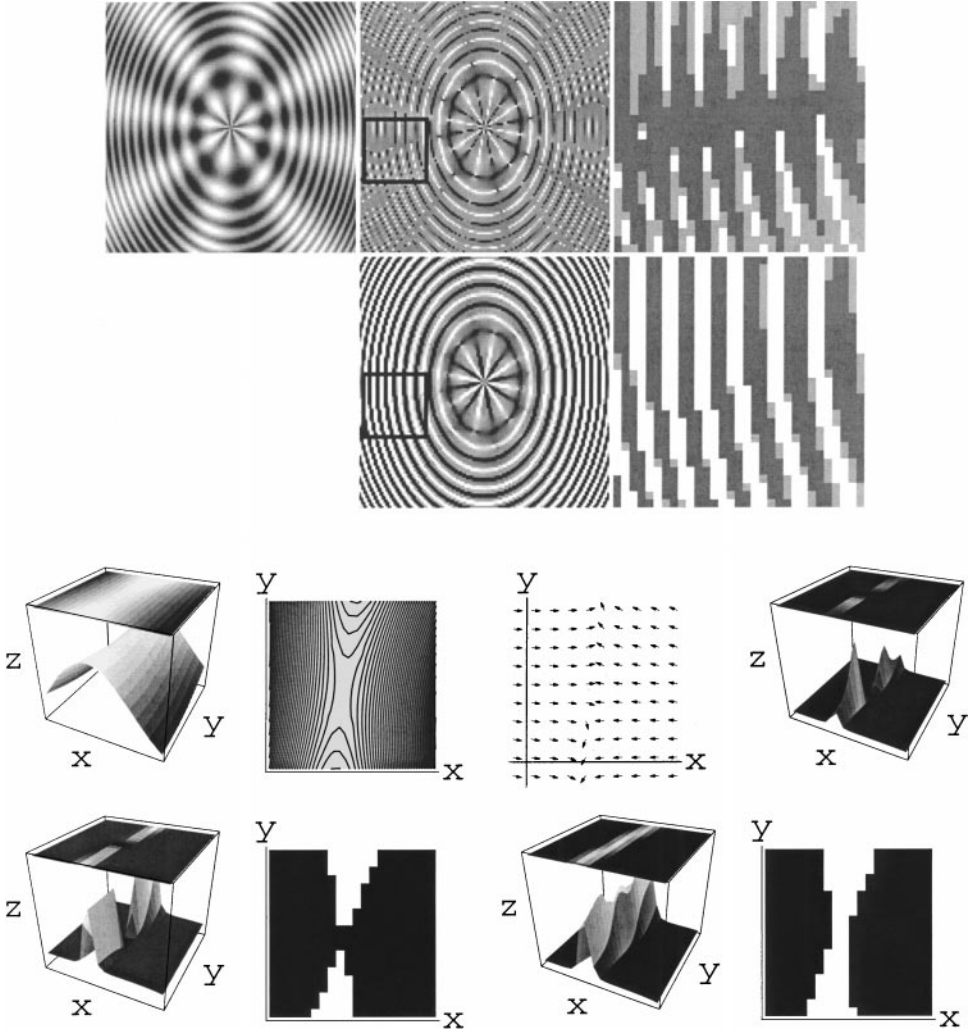


FIG. 13. From top to bottom and left to right: (a) $L(x, y) = \sin(60x^2 + 30y^2) + \sin(8 \arctan(y/x))$ sampled in $[-1, 1] \times [-1, 1]$ at a resolution of 128×128 pixels. (b) $T(\kappa, 1.0)$ with an ROI framed, where κ has been analytically computed and then sampled. (c) Zoom of the ROI. White lines: ridge-like creases after thresholding κ ; pixels where $\kappa > 0$ have been set to lighter gray, and where $\kappa < 0$ they are to darker. Notice the change of sign barrier. (d) $\bar{\kappa}^\diamond$. (e) Zoom of the previous ROI. Notice that there are no undesired changes of sign. (f) Relief from the samples of a zone of the test image. (g) Level curves revealing the presence of a generic ridge-like saddle. (h) Normalized gradient vector field of the relief. (i) κ after sampling its analytic expression. (j) $T(\kappa, 1.0)$. (k) In white, pixels where κ is positive (ridge-like). (l) $\bar{\kappa}^\diamond$. (m) In white, pixels where $\bar{\kappa}^\diamond$ is positive.

The eigenvector which corresponds to the highest eigenvalue of $\mathbf{S}(\mathbf{x}; \sigma_1)$, say $\mathbf{w}'(\mathbf{x}; \sigma_1)$, yields the *dominant gradient orientation* at \mathbf{x} , where “dominant” means inside the neighborhood $\mathcal{N}(\mathbf{x}; \sigma_1)$. In fact, a suitable choice for this window is a d -dimensional Gaussian, i.e., $\mathcal{N}(\mathbf{x}; \sigma_1) = G(\mathbf{x}; \sigma_1)$, which implies that a gradient vector at a point \mathbf{y} inside the neighborhood contributes to the computation of $\mathbf{S}(\mathbf{x}; \sigma_1)$ weighted as a function of the distance from \mathbf{x} to \mathbf{y} .

The eigenvector which corresponds to the lowest eigenvalue of $\mathbf{S}(\mathbf{x}; \sigma_1)$, namely, $\mathbf{v}'(\mathbf{x}; \sigma_1)$, yields the *dominant orientation* at \mathbf{x} , which is perpendicular to the *dominant gradient*

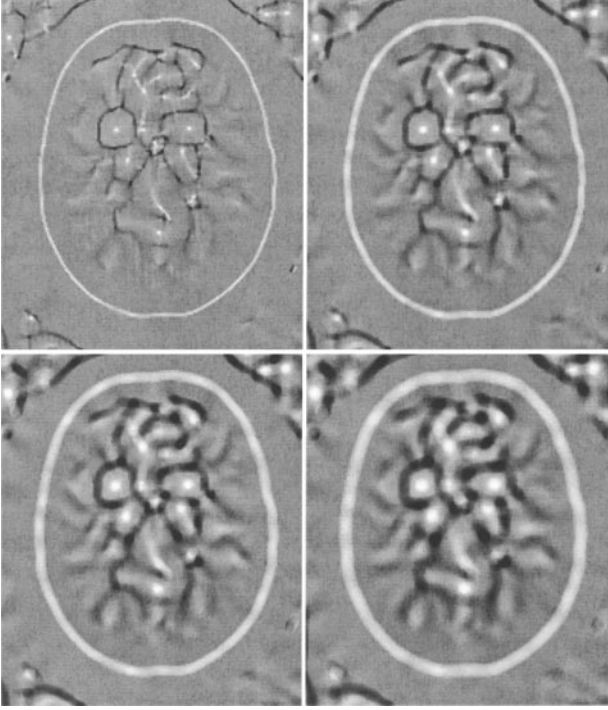


FIG. 14. From top to bottom and left to right: $\bar{\kappa}_2$ from the smoothed CT slice in Fig. 2, taking a circular neighborhood of radius 1, 2, 3, or 4, respectively.

orientation. Notice that the gradient of a function points toward the direction of maximum change, and the dominant orientation is perpendicular to this direction since anisotropy appears as similar gray values along one orientation and large perpendicular variations.

This analysis assumes that within each neighborhood there is a single dominant orientation. In order to verify this assumption, we introduce a normalized *confidence measure*: to each orientation we associate a real value $C \in [0, 1]$ which can be computed from the eigenvalues of the structure tensor. Similarity of the eigenvalues of the structure tensor implies isotropy, and, as a result, C should be close to zero. Therefore, denoting by $\lambda_1, \dots, \lambda_d$ the eigenvalues of \mathbf{S} , a logical choice consists of testing whether the sum of quadratic differences of them,

$$\lambda_{\Delta}(\mathbf{x}; \sigma_{\mathbf{I}}) = \sum_{i=1}^d \sum_{j=i+1}^d (\lambda_i(\mathbf{x}; \sigma_{\mathbf{I}}) - \lambda_j(\mathbf{x}; \sigma_{\mathbf{I}}))^2, \quad (21)$$

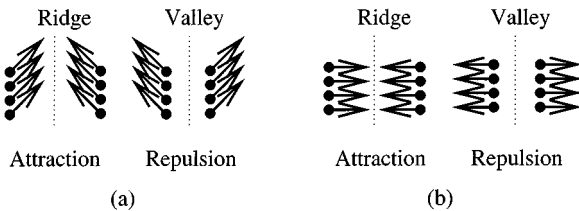


FIG. 15. Attraction and repulsion of vectors in (b) are higher than in (a).

exceeds a predefined threshold c characteristic for λ_Δ in the structure we want to enhance. A suitable function is [42]:

$$\mathbf{C}(\mathbf{x}; \sigma_I; c) = 1 - e^{-(\lambda_\Delta(\mathbf{x}; \sigma_I))^2 / 2c^2}. \quad (22)$$

Now we can obtain an enhanced creaseness measure by the following steps:

1. Compute the structure tensor field \mathbf{S} based on the gradient vector field \mathbf{w} . We will use a Gaussian neighborhood to compute \mathbf{S} . In the 3D case (to be used in Sections 4 and 5) this gives

$$\mathbf{S}(\mathbf{x}; \sigma_I; \sigma_D) = \begin{pmatrix} s_{11}(\mathbf{x}; \sigma_I; \sigma_D) & s_{12}(\mathbf{x}; \sigma_I; \sigma_D) & s_{13}(\mathbf{x}; \sigma_I; \sigma_D) \\ s_{12}(\mathbf{x}; \sigma_I; \sigma_D) & s_{22}(\mathbf{x}; \sigma_I; \sigma_D) & s_{23}(\mathbf{x}; \sigma_I; \sigma_D) \\ s_{13}(\mathbf{x}; \sigma_I; \sigma_D) & s_{23}(\mathbf{x}; \sigma_I; \sigma_D) & s_{33}(\mathbf{x}; \sigma_I; \sigma_D) \end{pmatrix}$$

$$\begin{aligned} s_{11}(\mathbf{x}; \sigma_I; \sigma_D) &= G(\mathbf{x}; \sigma_I) * (L_x(\mathbf{x}; \sigma_D)L_x(\mathbf{x}; \sigma_D)) \\ s_{12}(\mathbf{x}; \sigma_I; \sigma_D) &= G(\mathbf{x}; \sigma_I) * (L_x(\mathbf{x}; \sigma_D)L_y(\mathbf{x}; \sigma_D)) \\ s_{13}(\mathbf{x}; \sigma_I; \sigma_D) &= G(\mathbf{x}; \sigma_I) * (L_x(\mathbf{x}; \sigma_D)L_z(\mathbf{x}; \sigma_D)) \\ s_{22}(\mathbf{x}; \sigma_I; \sigma_D) &= G(\mathbf{x}; \sigma_I) * (L_y(\mathbf{x}; \sigma_D)L_y(\mathbf{x}; \sigma_D)) \\ s_{23}(\mathbf{x}; \sigma_I; \sigma_D) &= G(\mathbf{x}; \sigma_I) * (L_y(\mathbf{x}; \sigma_D)L_z(\mathbf{x}; \sigma_D)) \\ s_{33}(\mathbf{x}; \sigma_I; \sigma_D) &= G(\mathbf{x}; \sigma_I) * (L_z(\mathbf{x}; \sigma_D)L_z(\mathbf{x}; \sigma_D)). \end{aligned} \quad (23)$$

The new parameter σ_D denotes the standard deviation of the Gaussian kernel involved in the differentiation process needed to compute \mathbf{w} in a well-posed manner (Section 3.3). The parameter σ_D is called the *differentiation scale* in opposition to σ_I which is called the *integration scale*. The differentiation scale is tuned to the size of the objects whose orientation has to be determined, while the integration scale is tuned to the size of the neighborhood in which an orientation is dominant.

2. Perform the eigensystem analysis of \mathbf{S} . In this analysis, opposite directions are equally treated. Thus, in order to apply the divergence operator in the next step, we must assign a proper direction to the dominant gradient orientation \mathbf{w}' . To recover such direction we put \mathbf{w}' in the same quadrant in 2D, octant in 3D, etc., as \mathbf{w} . Then, we obtain the new vector field

$$\tilde{\mathbf{w}} = \text{sign}(\mathbf{w}'^t \cdot \mathbf{w})\mathbf{w}', \quad (24)$$

where the function $\text{sign}(x)$ takes the value $+1$ if $x > 0$, -1 if $x < 0$, and 0 if $x = 0$. In this way, attraction/repulsion of vectors is reinforced. As an example, Fig. 16 compares the normalized gradient vector field $\tilde{\mathbf{w}}$ versus the vector field $\tilde{\mathbf{w}}$.

3. Compute the new enhanced creaseness measure $\tilde{\kappa}_d$ (MLSEC-ST) as the following definition states:

DEFINITION 4 (MLSEC-ST). According to the divergence operator in Eq. (12), we define our MLSEC-ST operator for a discrete domain as:

$$\tilde{\kappa}_d = -\text{div}(\tilde{\mathbf{w}}). \quad (25)$$

We will use the term $\tilde{\kappa}^\diamond$ to denote the 2D MLSEC-ST measure based on the 4-adjacency divergence and $\tilde{\kappa}_M^\diamond$ for the 3D analogous.

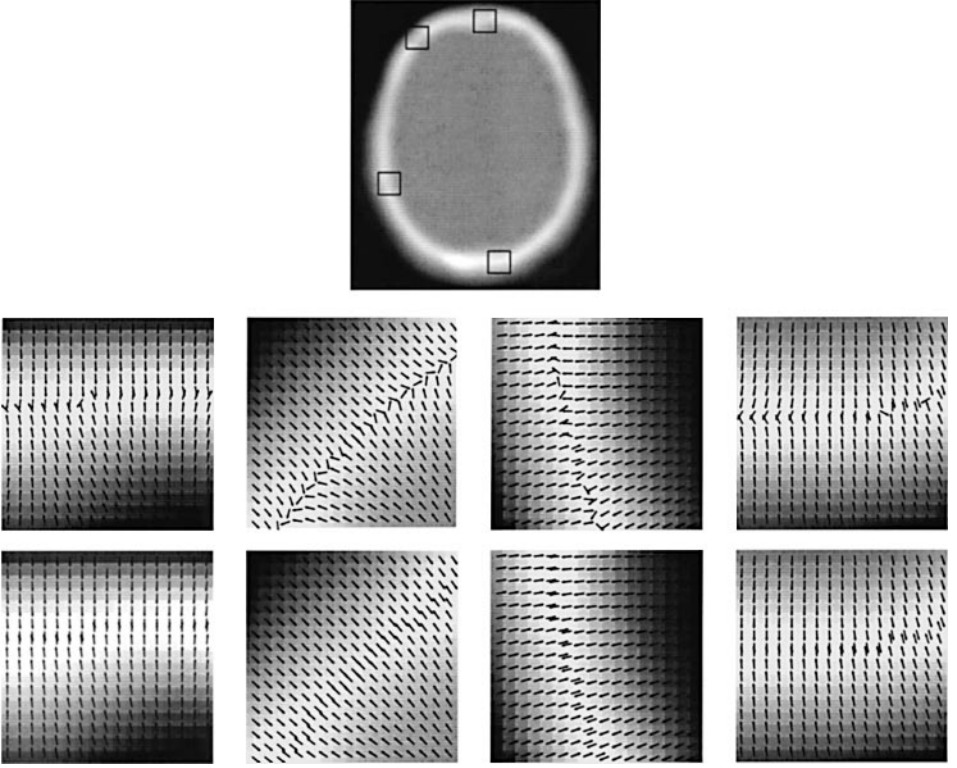


FIG. 16. First row: (a) Smoothed CT slice from Fig. 2 with four new ROIs framed. Second row: (b) Vector field $\tilde{\mathbf{w}}$ in the ROIs. Third row: (c) Vector field $\tilde{\mathbf{w}}$ according to the structure tensor analysis.

4. This is an optional step. Compute a suitable confidence measure \mathbf{C} to reduce creaseness in the structures we are not interested in. Then we can take $\tilde{\kappa}_d \mathbf{C}$ as the final creaseness measure.

Figure 17 shows the results obtained using $\tilde{\kappa}^\diamond$ and $-\tilde{\kappa}^\diamond \mathbf{C}$ to compare with κ , $L_{\mathbf{v}\mathbf{v}}$, and $\bar{\kappa}^\diamond$ of Figs. 2, 3, and 12. Notice how the MLSEC-ST measure does keep the good properties of the MLSEC due to the multilocal support of the divergence and exhibits a more homogeneous output. Besides, since $\tilde{\mathbf{w}}$ consists of an average direction of gradient vectors, the MLSEC-ST operator also has the same invariance properties as the MLSEC and the LSEC.

3.3. Computational Aspects

To obtain derivatives of a discrete image L in a well-posed manner [52, 14], we use the CFDs (Table I) of a Gaussian smoothed version of the image,

$$L_\alpha(\mathbf{x}; \sigma_D) \approx \delta_\alpha(L(\mathbf{x}) * G(\mathbf{x}; \sigma_D)), \quad \alpha \in \mathcal{X}_d, \quad (26)$$

where σ_D stands for the standard deviation of the Gaussian and δ_α for the CFD along the α axis. We perform the convolution in the spatial domain, taking advantage of the separability and symmetry properties of the Gaussian kernel to save time.

A method to calculate both κ in 2D and κ_M in 3D consists of computing the set of image derivatives, therefore \mathbf{w} , and then applying the respective equations. Analyzing the

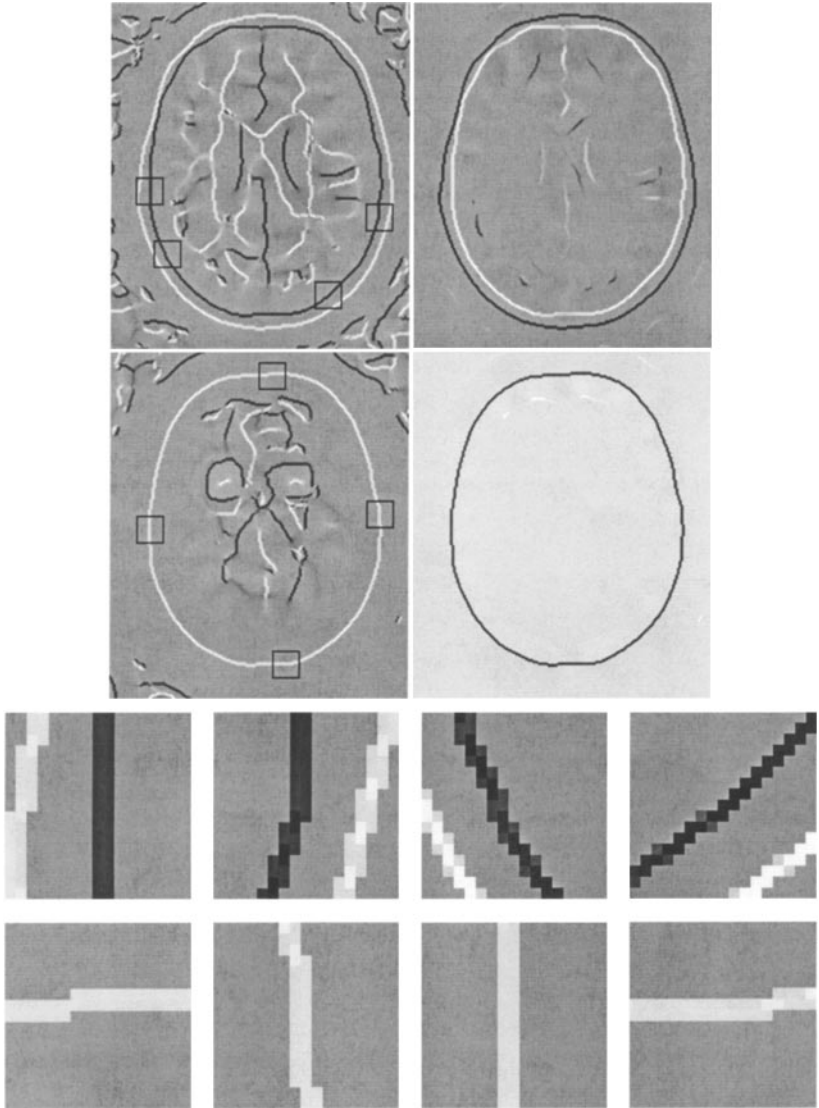


FIG. 17. First row from left to right: (a) $\tilde{\kappa}^\diamond$ ($\sigma_1 = 4.0$ pixels) of the smoothed MR slice in Fig. 2. (b) $-\tilde{\kappa}^\diamond C$ with $c = 1000$. Second row: (c) $\tilde{\kappa}^\diamond$ ($\sigma_1 = 4.0$ pixels) of the smoothed CT slice in Fig. 2. (d) $-\tilde{\kappa}^\diamond C$ with $c = 1000$. Third row: (e) Zoom of the ROIs of $\tilde{\kappa}^\diamond$ computed from the MR slice. Fourth row: (f) The same as for the CT.

computational requirements of $\tilde{\kappa}^\diamond$ and $\tilde{\kappa}_M^\diamond$, that is, the 2D and 3D MLSEC measures based on the smallest neighborhood when computing the divergence, we realize that even though they are multilocal measures they require less memory and operations than their local counterparts κ and κ_M (Table II). However, in 3D it is convenient to write an algorithm that scans the image voxel by voxel, computing the respective expression. The reason for this is that it saves memory: by first computing all the image derivatives involved in $\tilde{\kappa}_M^\diamond$ we need simultaneously seven float 3D images (Table II), which could mean a lot of memory. Therefore, we have adopted a voxel scanning approach [30] to minimize memory requirements and therefore disk access. On the other hand, when scanning pixel-by-pixel and computing $\tilde{\kappa}^\diamond$ or $\tilde{\kappa}_M^\diamond$ we have to buffer values to avoid the repetition of calculations.

TABLE II
Number of Operations at Each Pixel/Voxel to Compute κ and $\bar{\kappa}$ in 2D,
and κ_M and $\bar{\kappa}_M$ in 3D

	κ	$\bar{\kappa}^\diamond$	κ_M	$\bar{\kappa}_M^\diamond$
Maximum number of images simultaneously in memory	6	5	9	7
Additions and subtractions	15	6	33	10
Products and divisions	8	4	13	6
Square roots	1	1	1	1
Divisions by a constant	5	4	9	6

In practice this makes $\bar{\kappa}^\diamond$ and $\bar{\kappa}_M^\diamond$ slightly more time-consuming than κ and κ_M . Yet, the difference is small, as shown in Table III.

The computation of $\bar{\kappa}_d$ consumes many more resources than κ_d and $\bar{\kappa}_d$ (Table III) due to the eigensystem analysis and, mainly, the Gaussian averaging of the structure tensor components. In 2D we compute the eigenvalues of the structure tensor analytically; in 3D we are currently using the TQL method [46]. Again, to save memory, at the moment we use an implementation of $\bar{\kappa}^\diamond$ in 2D and $\bar{\kappa}_M^\diamond$ in 3D based on pixel-by-pixel scanning [30] (implementation available upon request, contact the first author).

When computing either the MLSEC or the MLSEC-ST it is clear that the larger the neighborhood \mathcal{W} used to implement the divergence operator, the larger the resources needed. Therefore, whenever it is possible, the best option is to keep on working with the smallest neighborhood, that is, the one based on the $2d$ -adjacency.

4. REGISTRATION OF CT AND MR HEAD VOLUMES

Image registration attempts to solve the problem that arises when two images taken at different times by different sensors or from different viewpoints need to be brought into spatial agreement in order to fuse their information. An upcoming application of image registration is in the field of medical images, especially after the introduction of 3D modalities.

We have focused on CT-MR registration because these modalities are widely available and provide partially complementary information (CT depicts bones accurately, while MR

TABLE III
CPU Time in a 200-MHz Pentium Pro PC with 128 MB of RAM Memory under Linux OS

Image dimensions	Gaussian smoothing ($\sigma_D = 4.0$)		L_{vv}	κ	$\bar{\kappa}^\diamond$	$\bar{\kappa}^\diamond$ ($\sigma_1 = 4.0$)
	L_{pp} or L_{qq}	κ_M				
256 × 256	0.09 s	0.058 s	0.058 s	0.072 s	0.6 s	
512 × 512	0.37 s	0.24 s	0.24 s	0.28 s	2.4 s	
128 × 128 × 84	2 s	7 s	1.8 s	2.1 s	80 s	
250 × 250 × 180	18 s	75 s	23 s	23.3 s	720 s	

differentiates soft tissues). First, multisensor registration methods used physical markers visible in both modalities to provide reference points, but they were manual and had the drawbacks of lacking retrospectiveness and not being patient friendly.

Currently, we are developing an automatic registration method for CT and MR head volumes, which is similar to that introduced by Dr. van den Elsen in [11]. It is based on the fact that the skull is visible in both CT and MR brain images. The signal produced by the bone is strong in CT, but weak in MR, in such a way that the skull forms a ridge structure in the CT volume and a valley in the MR. Moreover, since the skull is undeformable, only rigid transformations need to be considered. Thus, only six parameters must be found, three rotation angles and a 3D translation vector. Scaling factors are known from the acquisition system settings (image dimensions and field of view).

Let us briefly review the steps of our registration procedure. The first one consists of scaling the CT and MR images to have voxels of the same size. Second, we must extract the center of the skull from both the CT and the MR scaled images. Since the skull in the CT volume appears as a ridge structure, we can use a ridge operator working in 3D to extract the center of the skull. Let us term as \mathcal{R} the response of such an operator. Analogously, we can use a valley operator working in 3D to extract its center. Let \mathcal{V} be its response. The last step consists of iteratively transforming \mathcal{R} until it becomes properly aligned with \mathcal{V} . This is a difficult task due to the huge size of the data and the high dimensionality of the space of transformations. To overcome the first drawback we use a pyramidal search (\mathcal{R} and \mathcal{V} are sampled to generate a multiresolution pyramid), following Dr. van den Elsen's proposal. To overcome the second drawback we incorporate an optimized search at each level of the pyramid, in this case, unlike Dr. van den Elsen who used an exhaustive search which, in general, is more time-consuming.

If we assume that \mathcal{R} has the same origin of coordinates as \mathcal{V} , we can state that \mathcal{R} and \mathcal{V} are perfectly aligned if at any voxel \mathbf{i} we have $\mathcal{R}(\mathbf{i}) = \mathcal{V}(\mathbf{i})$. Obviously, this is an ideal situation. In practice, a reliable method to evaluate how \mathcal{R} resembles \mathcal{V} consists of correlating them. The higher the correlation the better the alignment. The correlation performs well, but we have to be careful during the search for the aligning transform to avoid being caught in local maxima of the correlation between \mathcal{R} and \mathcal{V} .

It has been experimentally seen that, if we use the correlation operator to compare \mathcal{R} and \mathcal{V} , a reliable approach consists of working with creaseness measures, that is, \mathcal{R} being a 3D ridgeness measure of the CT volume and \mathcal{V} a valleyiness measure of the 3D MR volume. Of course, with this approach good contrast, continuity, and homogeneity are quite desirable properties to avoid noisy local maxima of the correlation between \mathcal{R} and \mathcal{V} , and to generate a meaningful multiresolution pyramid of both measures.

In her work, Dr. van den Elsen proposed the pair of 3D operators L_{pp} and L_{qq} introduced in Section 2.1. As can be seen in Fig. 18, both measures present discontinuities along the skull, and they do not have a homogeneous response. Figure 19 shows the results obtained with $\tilde{\kappa}_M^\diamond$ and $C\tilde{\kappa}_M^\diamond$. We observe that the response of $\tilde{\kappa}_M^\diamond$ is continuous and more homogeneous along the skull of both the CT image and the MR image. Moreover, its computation is less time-consuming than that of L_{pp} and L_{qq} (Table III). However, it is clear that $C\tilde{\kappa}_M^\diamond$ is the best option.

Concerning the way to compare our registration method with other existing ones, we are currently obtaining results to be evaluated in the framework of the "Evaluation of Retrospective Image Registration" project conducted by Dr. Fitzpatrick and Dr. West at Vanderbilt University. This project has as its primary goal the blinded evaluation of a group of retrospective image registration techniques using as a gold standard a prospective,

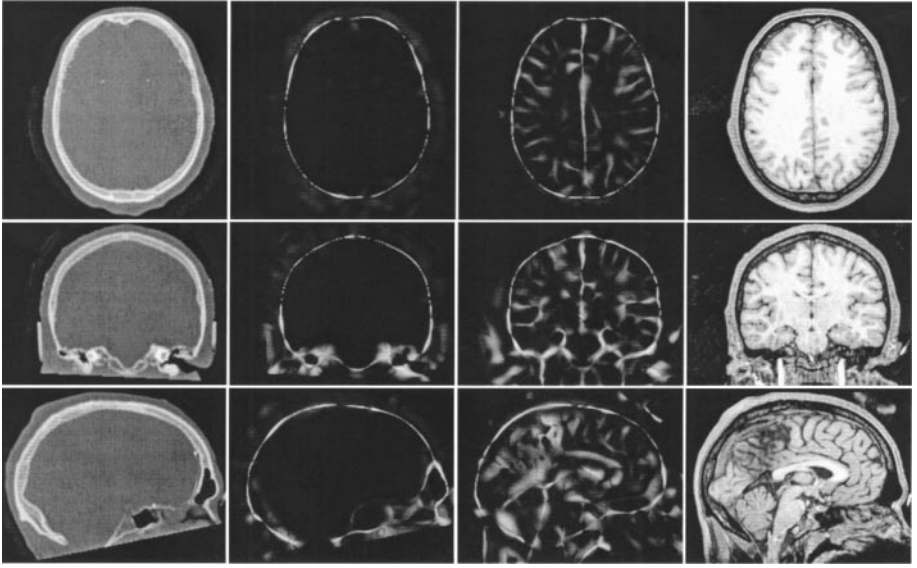


FIG. 18. From the left column to the right one: (a) Transversal, coronal, and sagittal slices of a $250 \times 250 \times 180$ CT volume with cubic voxels. (b) $-L_{pp} > 0$ from the CT volume. (c) $L_{qq} > 0$ from the MR volume. (d) Slices of a $250 \times 250 \times 180$ MR image with cubic voxels. The operators were applied after the Gaussian smoothing of the images, with $\sigma_D = 4.0$ pixels.

marker-based registration method. Its first results have been already published [57, 13]. According to them, it seems that one of the best algorithms is that of Studholme, Hill and Hawkes [51], and it is based on the *mutual information* (MI) technique [5, 56]. Therefore, we decided to start by comparing our results directly with those of this algorithm. This

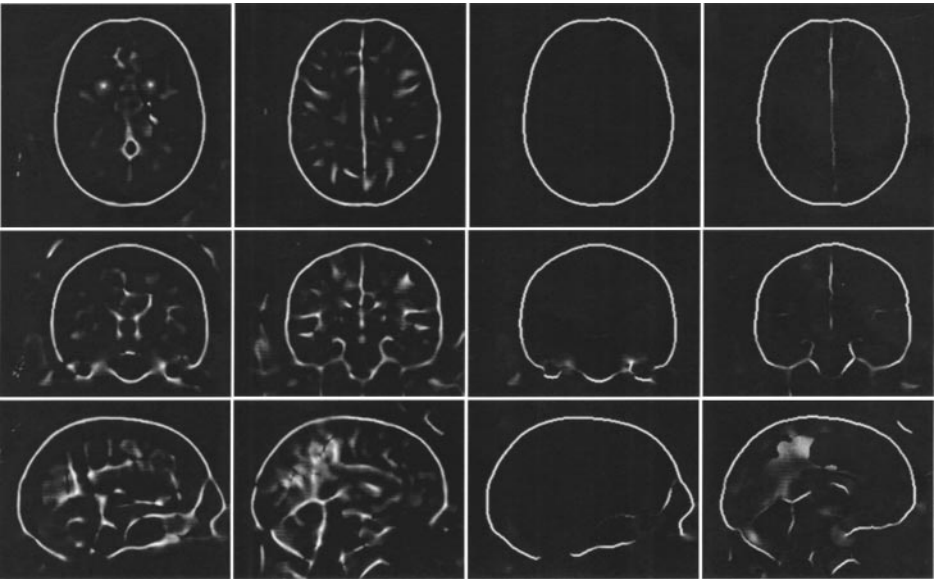


FIG. 19. From the left column to the right one: (a) $\tilde{\kappa}_M^\diamond > 0$ from the CT image in the first column of Fig. 18. (b) $-\tilde{\kappa}_M^\diamond > 0$ from the MR image in the last column of Fig. 18. (c) $C\tilde{\kappa}_M^\diamond > 0$ from the same CT image. (d) $-C\tilde{\kappa}_M^\diamond > 0$ from the same MR image. In both (c) and (d) the same specific parameters were used, namely, $\sigma_1 = 4.0$ pixels and $c = 1000$. The operators were applied after the Gaussian smoothing of the images, with $\sigma_D = 4.0$ pixels.

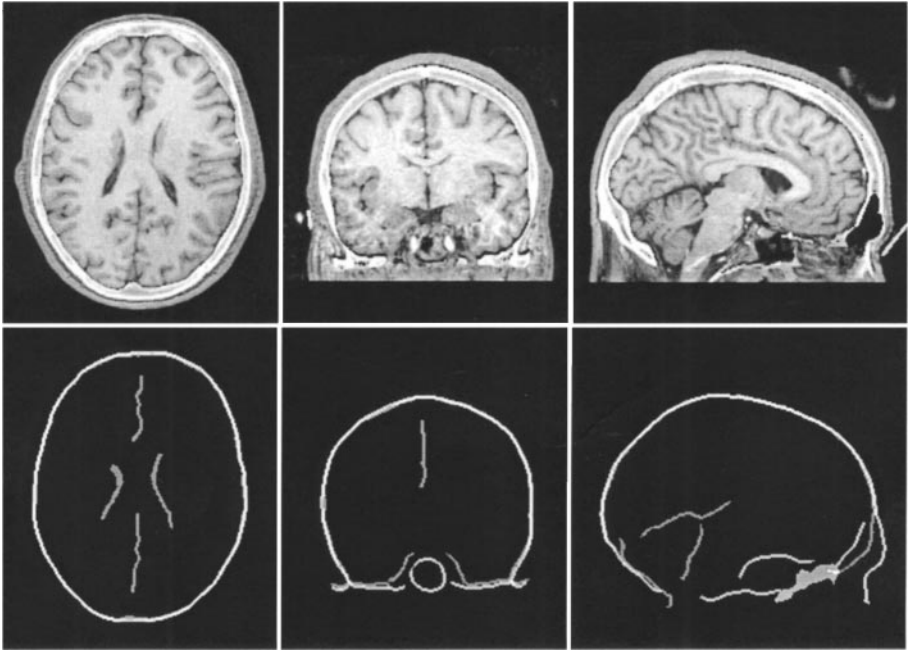


FIG. 20. Top row: (a) Example where the bone of the CT volume has been fused with the MR data after our registration process. Bottom row: (b) Location of the creases obtained by thresholding the MLSEC-ST-based ridgeness and valleyiness measures from the CT and MR volumes, respectively, at their final positions. The darker gray indicates ridges from the CT data, the medium gray indicates valleys from the MR data, and white indicates spatial coincidence of these ridges and valleys.

study is presented in [29], where the comparison indicates that our method is more robust (reliability under adverse conditions) than the MI with comparable accuracy. Figure 20 shows a fusion example after registering the CT and MR volumes of Fig. 18 using our method.

5. ANALYSIS OF THE ORIENTATION OF TRABECULAR BONE PATTERNS

Human bone can be classified as cortical or trabecular, depending on its relative density [18]. Most bones are built of both types; the cortical part forms a dense shell, in contrast with the mesh appearance of the trabecular part, which covers the inner side of the shell. There is increasing clinical evidence that measures of architecture in the trabecular bone pattern play an important role in the loss of bone strength, e.g., in bone diseases like osteoporosis. Since means of prevention and treatment of osteoporosis are now available [28], tools for *in vivo* diagnosis of relevant bone properties are invaluable.

The trabecular pattern is visible at resolutions which can be appreciated from conventional CT images. A neutron diffraction study by Bacon *et al.* [1] confirmed that there exists a high correlation between the direction of individual trabeculae and routes of stress, which are apparent at a larger scale and are related to mechanical loading in the body according to [18]. Our aim is to determine these stress routes from 3D noninvasively obtained data, in order to study the relationships between structure, mechanical loading, and, in pathological cases, malgrowth.

The routes of stress can be seen as an oriented texture in 3D images. Since they appear at scales which are considerably higher than the size of individual trabeculae and vary within the human skeleton, in [43, 42, 41] we used a multiscale texture analysis method based on the structure tensor. This method, let us call it method 1, consists of the following steps:

1. Analysis of the trabeculae. At each voxel \mathbf{i} of the image:
 - (a) Obtain the eigenvectors and eigenvalues of $\mathbf{S}(\mathbf{i}; \sigma_{\mathbf{I}}^{\text{trab}}; \sigma_{\mathbf{D}}^{\text{trab}})$, that is, the structure tensor with parameters tuned to the trabecular pattern.
 - (b) Take the dominant orientation $\mathbf{v}'(\mathbf{i}; \sigma_{\mathbf{I}}^{\text{trab}}; \sigma_{\mathbf{D}}^{\text{trab}})$.
 - (c) Compute $\mathbf{C}(\mathbf{i}; \sigma_{\mathbf{I}}^{\text{trab}}; \sigma_{\mathbf{D}}^{\text{trab}}; c^{\text{trab}})$.
2. The dominant orientation $\mathbf{v}'(\mathbf{i}; \sigma_{\mathbf{I}}^{\text{trab}}; \sigma_{\mathbf{D}}^{\text{trab}})$ is considered as a meaningful dominant orientation of the trabecular pattern if $\mathbf{C}(\mathbf{i}; \sigma_{\mathbf{I}}^{\text{trab}}; \sigma_{\mathbf{D}}^{\text{trab}}; c^{\text{trab}}) > t^{\text{trab}}$, where t^{trab} is a given threshold value on $[0, 1]$, which is the range of the confidence measure.

With this method, however, cortical bone and intertrabecular space yield high confidence. The main problem is the cortical bone influence, which manifests itself in two different ways:

- **Pa:** Orientations due to cortical bone and intertrabecular space are included in the orientations of the voxels passing the test of step 2. Therefore, measures that look for a global preferred orientation, such as a histogram of orientations, are affected by them.
- **Pb:** If we choose a large $\sigma_{\mathbf{I}}^{\text{trab}}$ with the purpose of obtaining a more global measure of the trabeculae orientation, then, since cortical bone is a highly oriented structure, it will have a high influence in the trabeculae orientations that are “at a distance lower than $\sigma_{\mathbf{I}}^{\text{trab}}$.”

In order to overcome these problems we have revised method 1. Our main aim was to inhibit cortical bone effects without performing a fine segmentation, which in general is a nontrivial task since trabecular and cortical bone produce a response of similar gray-level, so they cannot be distinguished from each other by simply thresholding. With this aim, we observe that cortical bone produces a ridge structure in CT images. Therefore, as in the case of CT/MR registration, we can approximately segment cortical bone by using the MLSEC-ST, but with a divergence operator based on a neighborhood of an appropriate size (Fig. 14). In addition, to avoid intertrabecular space influence, we only consider the orientations at the center of the trabeculae (this is like saying that the dominant orientation of a cylinder is that of its central axis). We term the method deriving from this idea as method 2, which is adapted here from [32] in order to better appreciate the contribution of our MLSEC-ST operator in this application:

1. Analysis of the cortical bone. At each voxel \mathbf{i} of the image, compute the weighted creaseness measure $\tilde{\kappa}_{\mathbf{M}}(\mathbf{i}; \sigma_{\mathbf{I}}^{\text{cort}}; \sigma_{\mathbf{D}}^{\text{cort}})\mathbf{C}(\mathbf{i}; \sigma_{\mathbf{I}}^{\text{cort}}; \sigma_{\mathbf{D}}^{\text{cort}}; c^{\text{cort}})$ as described in Section 3.2, where the parameters are tuned to the cortical bone size and contrast. In this case, given a radius ρ , we will use the points of the boundary of a discrete sphere to discretize the divergence according to Eq. (12). Let us refer by $\tilde{\kappa}_{\mathbf{M}}^{\rho}(\mathbf{i}; \sigma_{\mathbf{I}}^{\text{cort}}; \sigma_{\mathbf{D}}^{\text{cort}})$ to the MLSEC-ST operator computed by using such a spherical neighborhood. Then, as we have already seen in Fig. 14, by taking a sufficiently large ρ , we can obtain high creaseness values along the whole cortical bone, not only along its center.
2. Analysis of the trabeculae. At each voxel \mathbf{i} of the image:
 - (a) Obtain the eigenvectors and eigenvalues of $\mathbf{S}(\mathbf{i}; \sigma_{\mathbf{I}}^{\text{trab}}; \sigma_{\mathbf{D}}^{\text{trab}})$.
 - (b) Take $\mathbf{v}'(\mathbf{i}; \sigma_{\mathbf{I}}^{\text{trab}}; \sigma_{\mathbf{D}}^{\text{trab}})$.
 - (c) Compute $\tilde{\kappa}_{\mathbf{M}}^{\rho}(\mathbf{i}; \sigma_{\mathbf{I}}^{\text{trab}}; \sigma_{\mathbf{D}}^{\text{trab}})\mathbf{C}(\mathbf{i}; \sigma_{\mathbf{I}}^{\text{trab}}; \sigma_{\mathbf{D}}^{\text{trab}}; c^{\text{trab}})$ as described in Section 3.2.

3. Combine the trabecular and the cortical bone analysis. Given the threshold values t^{trab} and t^{cort} running on $[0, 3]$ (ridginess range of the MLSEC-ST in 3D), if $\tilde{\kappa}_M^\diamond(\mathbf{i}; \sigma_I^{\text{trab}}; \sigma_D^{\text{trab}}) \mathbf{C}(\mathbf{i}; \sigma_I^{\text{trab}}; \sigma_D^{\text{trab}}; c^{\text{trab}}) > t^{\text{trab}}$ and $\tilde{\kappa}_M^\rho(\mathbf{i}; \sigma_I^{\text{cort}}; \sigma_D^{\text{cort}}) \mathbf{C}(\mathbf{i}; \sigma_I^{\text{cort}}; \sigma_D^{\text{cort}}) < t^{\text{cort}}$, then $\mathbf{v}'(\mathbf{i}; \sigma_I^{\text{trab}}; \sigma_D^{\text{trab}})$ is considered as a meaningful dominant orientation of the trabecular pattern.

With this method only trabecular bone is taken into account, that is, the dominant orientation of this pattern is neither artificially reinforced nor disturbed by the intertrabecular

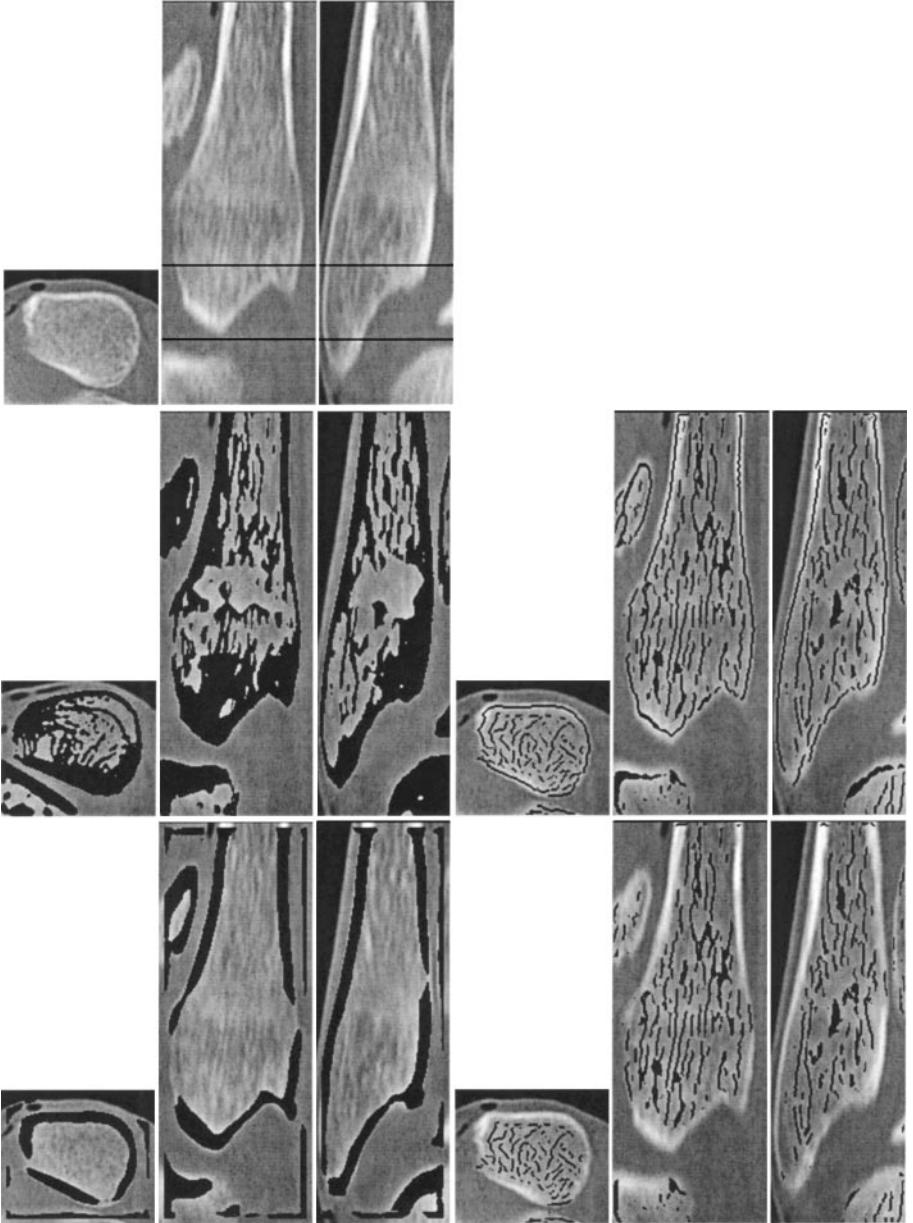


FIG. 21. From top to bottom and left to right: (a) Transversal sagittal and coronal sections of the bottom of a fibula. (b) In black, voxels taken into account by method 1. (c) Ridges from $\tilde{\kappa}_M^\diamond \mathbf{C}$ in method 2. (d) Ridges from $\tilde{\kappa}_M^\rho \mathbf{C}$ in method 2. (e) Voxels taken into account by method 2, that is, voxels selected in (c) but not in (d).

space or the cortical bone, and dominant orientations that do not correspond to trabeculae are removed provided σ_1^{trab} is kept sufficiently small. Therefore, this scheme solves **Pa**. Because in this application we wanted to evaluate the effect of **Pa** and **Pb** separately, we started by solving just **Pa**, and **Pb** will be solved in future work.

Now we illustrate the 3D results by concentrating the analysis on the bottom of the fibula (Fig. 21a), imaged *in vitro* by means of a CT scanner with realistic *in vivo* settings, pixel resolution of 0.25×0.25 mm and slice thickness of 0.8 mm. To perform this analysis we first interpolate the data to get cubic voxels. Since the bone is mainly oriented vertically with respect to the image coordinates we expect to obtain this orientation as the most significant. We have used the following parameters for method 1: $\sigma_D^{\text{trab}} = 0.5$, $\sigma_1^{\text{trab}} = 3.0$, and $c^{\text{trab}} = 2500$. With method 2 the parameters were: $\sigma_1^{\text{cort}} = 4.0$, $\sigma_D^{\text{cort}} = 3.0$, $c^{\text{cort}} = 1000$, $\rho = 5$, $\sigma_D^{\text{trab}} = 0.5$, $\sigma_1^{\text{trab}} = 3.0$, and $c^{\text{trab}} = 1000$. In these experiments we have taken the ridges in step 2 of method 2 as the loci where $\tilde{\kappa}_M^\diamond \mathbf{C} > 0.5$, and the ridge areas of step 1 as the loci where $\tilde{\kappa}_M \mathbf{C} > 0.4$. In method 1 we have taken as relevant orientations those

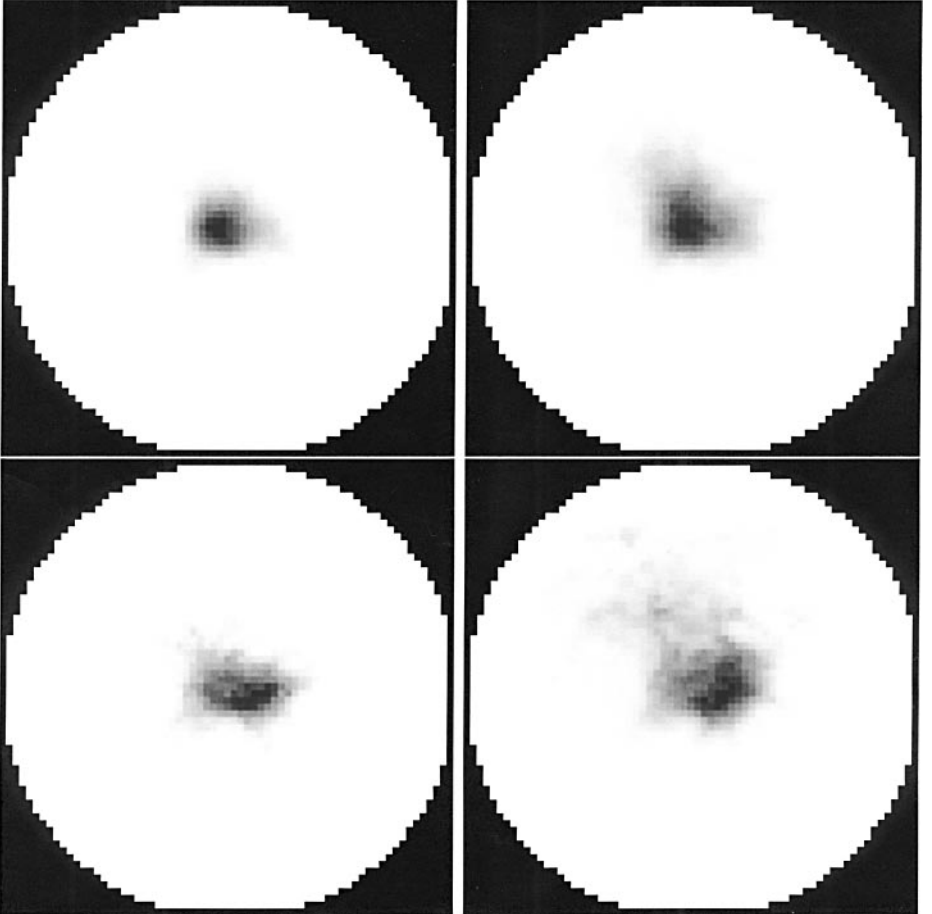


FIG. 22. From top to bottom and left to right: (a) Orthographic projection of a normalized histogram of 3D orientations (superior hemisphere discretized into 62×62 cells) from the trabecular bone in the fibula, according to method 2. Dark denotes a high incidence. (b) The same as for method 1. (c) Projection only takes into account the planes framed in Fig. 21a, according to method 2. (d) The same as for method 1.

placed at points where $C > 0.5$. Figure 21b shows the voxels whose orientations will be taken into account by method 1, and Fig. 21e shows the ones taken into account by method 2. We visualize the 3D anisotropy in the trabecular structure in Figs. 22a, and 22b. Both methods reveal that the main orientation is slightly off the vertical axis, which runs along the longitudinal axis of the fibula. Method 1 gives a more noisy result than method 2 because cortical bone orientations do count. However, in this case the main orientation is still found by method 1 due to the fact that we analyze a large part of the fibula and the cortical bone is oriented mainly as the trabeculae, and only more at the bottom of the fibula do these orientations differ. Instead, taking into account only orientations from the planes marked in Fig. 21a, we appreciate a major difference between the two methods (Figs. 22c and 22d).

6. SUMMARY

The level-set extrinsic curvature (LSEC) is a creaseness measure for d -dimensional images that acts as an approximation of medialness for gray-level objects. In this paper we have first identified two problems that it presents when used as a tool for image analysis, the badly dynamic range and the discontinuities of the response. Related creaseness measures, like L_{vv} in 2D or κ_M , L_{pp} , and L_{qq} in 3D, also present discontinuities and lack of homogeneity. We have analyzed these problems and reached the conclusion that they are due to the local definition of the LSEC itself. Therefore, we have proposed an alternative multilocal operator based on the LSEC idea, the MLSEC, which has been directly designed for the discrete domain. It has been shown that this new operator avoids the problems of the LSEC. We have also proposed an extension of the MLSEC which adapts the structure tensor from oriented texture analysis to enhance the response of the MLSEC. This new operator, the MLSEC-ST, can be combined with its associated confidence measure to give an even cleaner creaseness measure along the center of the objects of interest.

Results have been shown in the context of two applications on 3D images, namely, the registration of CT and MR head volumes and the computation of trabecular bone dominant orientations from CT volumes. In the first case, our MLSEC-ST measure has been shown to be ideal as a common feature from CT and MR volumes to perform the registration. Current results indicate that the obtained overall accuracy is in most cases sub-pixel and comparable to that achieved by the mutual information method. In the second case, we have presented a new method to define trabecular orientation in a quantitative robust manner. This method presents as an improvement, with respect to the previously existing operator (also based on the structure tensor analysis), the use of the MLSEC-ST operator to reduce the influence in the analysis of both the cortical bone and the intertrabecular space, which are also strongly oriented structures.

Finally, we have to mention that in this paper we have concentrated on showing results of the MLSEC-ST in 3D applications. In [30] we show how the MLSEC gives satisfactory results in the context of other applications.

APPENDIX A

Expression in Terms of Cartesian Coordinates of the LSEC in 2D and 3D

In this appendix we show how to obtain Eqs. (3) and (4) from Eq. (2). According to the Einstein summation convention (if an index occurs twice in a given term or in multiplicative

terms, a summation over all possible index values is assumed, in this case, from 1 to d), we have

$$\begin{aligned} L_\alpha L_\beta L_{\alpha\beta} &= \sum_{i=1}^d \sum_{j=1}^d L_{x^i} L_{x^j} L_{x^i x^j}, \\ L_\alpha L_\alpha L_{\beta\beta} &= \left(\sum_{i=1}^d L_{x^i} L_{x^i} \right) \left(\sum_{j=1}^d L_{x^j x^j} \right) = \sum_{i=1}^d L_{x^i}^2 \left(\sum_{j=1}^d L_{x^j x^j} \right), \\ L_\gamma L_\gamma &= \sum_{i=1}^d L_{x^i} L_{x^i} = \sum_{i=1}^d L_{x^i}^2. \end{aligned}$$

Then, using Cartesian coordinates in 2D ($x^1 = x, x^2 = y$), we have

$$\begin{aligned} L_\alpha L_\beta L_{\alpha\beta} &= L_x^2 L_{xx} + 2L_x L_y L_{xy} + L_y^2 L_{yy}, \\ L_\alpha L_\alpha L_{\beta\beta} &= L_x^2 (L_{xx} + L_{yy}) + L_y^2 (L_{xx} + L_{yy}), \\ L_\alpha L_\beta L_{\alpha\beta} - L_\alpha L_\alpha L_{\beta\beta} &= 2L_x L_y L_{xy} - L_x^2 L_{yy} - L_y^2 L_{xx}, \\ L_\gamma L_\gamma &= L_x^2 + L_y^2, \end{aligned}$$

and in 3D ($x^1 = x, x^2 = y, x^3 = z$)

$$\begin{aligned} L_\alpha L_\beta L_{\alpha\beta} &= 2(L_x L_y L_{xy} + L_x L_z L_{xz} + L_y L_z L_{yz}) \\ &\quad + L_x^2 L_{xx} + L_y^2 L_{yy} + L_z^2 L_{zz}, \\ L_\alpha L_\alpha L_{\beta\beta} &= L_x^2 (L_{xx} + L_{yy} + L_{zz}) + L_y^2 (L_{xx} + L_{yy} + L_{zz}) \\ &\quad + L_z^2 (L_{xx} + L_{yy} + L_{zz}), \\ L_\alpha L_\beta L_{\alpha\beta} - L_\alpha L_\alpha L_{\beta\beta} &= 2(L_x L_y L_{xy} + L_x L_z L_{xz} + L_y L_z L_{yz}) - L_x^2 (L_{yy} + L_{zz}) \\ &\quad - L_y^2 (L_{xx} + L_{zz}) - L_z^2 (L_{xx} + L_{yy}), \\ L_\gamma L_\gamma &= L_x^2 + L_y^2 + L_z^2. \end{aligned}$$

Of course, we are always supposing continuity of the partial derivatives, and thereby $L_{x^i x^j} = L_{x^j x^i}$. Finally, by mere substitution in Eq. (2) of the 2D and 3D Cartesian formulae we obtain Eqs. (3) and (4), respectively.

APPENDIX B

The LSEC in Terms of the Gradient Vector Field

The aim of this appendix is to prove the equality of Eq. (9) given Eqs. (2), (7), and (8). The normalized gradient vector is expressed in terms of its components as $\bar{\mathbf{w}} = (L_{x^1}, \dots, L_{x^d}) / (\sum_{j=1}^d L_{x^j}^2)^{1/2}$. Therefore, to prove Eq. (9) we have to show that

$$\frac{\sum_{i=1}^d \sum_{j=1}^d L_{x^i} L_{x^j} L_{x^i x^j} - \sum_{i=1}^d L_{x^i}^2 \left(\sum_{j=1}^d L_{x^j x^j} \right)}{\left(\sum_{i=1}^d L_{x^i}^2 \right)^{3/2}} = - \sum_{i=1}^d \frac{\partial}{\partial x^i} \left(\frac{L_{x^i}}{\left(\sum_{j=1}^d L_{x^j}^2 \right)^{1/2}} \right),$$

where the right-hand side of Eq. (2) has been translated into the “summational language” according to Appendix A. This equality can be proved by developing its right-hand side as follows:

$$\begin{aligned}
& - \sum_{i=1}^d \frac{\partial}{\partial x^i} \left(\frac{L_{x^i}}{(\sum_{j=1}^d L_{x^j}^2)^{1/2}} \right) \\
&= - \sum_{i=1}^d \frac{L_{x^i x^i} (\sum_{j=1}^d L_{x^j}^2)^{1/2} - L_{x^i} \frac{1}{2} (\sum_{j=1}^d L_{x^j}^2)^{-1/2} 2 (\sum_{j=1}^d L_{x^j} L_{x^i x^j})}{\sum_{j=1}^d L_{x^j}^2} \\
&= \sum_{i=1}^d \frac{L_{x^i} (\sum_{j=1}^d L_{x^j} L_{x^i x^j}) - L_{x^i x^i} (\sum_{j=1}^d L_{x^j}^2)}{(\sum_{j=1}^d L_{x^j}^2)^{3/2}} \\
&= \frac{\sum_{i=1}^d L_{x^i} (\sum_{j=1}^d L_{x^j} L_{x^i x^j}) - \sum_{i=1}^d L_{x^i x^i} (\sum_{j=1}^d L_{x^j}^2)}{(\sum_{i=1}^d L_{x^i}^2)^{3/2}} \\
&= \frac{\sum_{i=1}^d \sum_{j=1}^d L_{x^i} L_{x^j} L_{x^i x^j} - \sum_{j=1}^d \sum_{i=1}^d L_{x^i x^j} L_{x^j}^2}{(\sum_{i=1}^d L_{x^i}^2)^{3/2}} \\
&= \frac{\sum_{i=1}^d \sum_{j=1}^d L_{x^i} L_{x^j} L_{x^i x^j} - \sum_{i=1}^d L_{x^i}^2 (\sum_{j=1}^d L_{x^j}^2)}{(\sum_{i=1}^d L_{x^i}^2)^{3/2}}.
\end{aligned}$$

■

ACKNOWLEDGMENTS

This research has been partially funded by Spanish CICYT projects TIC97-1134-C02-02 and TAP96-0629-C04-03. Special thanks to Dr. Petra van den Elsen for providing the CT and MR head volumes. The authors kindly acknowledge also Dr. Wiro Niessen and Dr. Bart ter Haar Romeny from the ISI at the Utrecht University Hospital, with whom we are working on the trabecular bone project. We also thank Dr. Derek Hill and Dr. David Hawkes, from the Computational Imaging Science Group in Radiological Sciences, UMDS, Guy’s and St. Thomas’ Hospital, for allowing us access to the mutual information registration software (written by Dr. Collin Studholme).

REFERENCES

1. G. E. Bacon, P. J. Bacon, and R. K. Griffiths, The orientation of apatite crystals in bone, *J. Appl. Crystallogr.* **12**, 1979, 99–103.
2. S. Beucher and F. Meyer, The morphological approach to segmentation: The watershed transform, in *Mathematical Morphology in Image Processing* (D. Dougherty, Ed.), pp. 433–481, Dekker, New York, 1993.
3. J. Bigun, G. Granlund, and J. Wiklund, Multidimensional orientation estimation with applications to texture analysis and optical flow, *IEEE Trans. Pattern Anal. Machine Intell.* **13**, 1991, 775–790.
4. A. Cayley, On contour and slope lines, *London, Edinburgh and Dublin Philos. Mag. J. Sci.* **18**, 1859, 264–268.
5. A. Collignon, F. Maes, D. Delaere, D. Vandermeulen, P. Suetens, and G. Marchal, Automated multi-modality image registration based on information theory, in *Information Processing in Medical Imaging* (Y. Bizais, C. Barillot, and R. Di Paola, Eds.), pp. 263–274, Kluwer Academic, Dordrecht, 1995.
6. J. Crowley and A. Parker, A representation for shape based on peaks and ridges in the difference of low-pass transform, *IEEE Trans. Pattern Anal. Machine Intell.* **6**, 1984, 156–170.
7. M. de Saint-Venant, Surfaces à plus grande pente constituées sur des lignes courbes, *Bull. Soc. Philomath. Paris* (March 6th), 1852, 24–30.
8. J. Desmet and G. Govers, Comparison of routing algorithms for digital elevation models and their implications for predicting ephemeral gullies, *Internat J. Geograph. Inform. Systems* **10**, 1996, 311–331.

9. M. do Carmo, Ed., *Differential Geometry of Curves and Surfaces*, Prentice Hall, New York, 1976.
10. D. Eberly, R. Gardner, B. Morse, S. Pizer, and C. Scharlach, Ridges for image analysis, *J. Math. Imaging Vision* **4**, 1994, 353–373.
11. P. van den Elsen, J. Maintz, E.-J. Pol, and M. Viergever, Automatic registration of CT and MR brain images using correlation of geometrical features, *IEEE Trans. Medical Imaging* **14**, 1995, 384–396.
12. J. Fairfield and P. Leymarie, Drainage networks from grid digital elevation models, *Water Resources Res.* **27**, 1991, 709–717.
13. J. Fitzpatrick and J. West, A blinded evaluation and comparison of image registration methods, in *Empirical Evaluation Techniques in Computer Vision* (K. Bowyer and P. Phillips, Eds.), pp. 12–27, IEEE Computer Soc., 1998.
14. L. Florack, B. ter Haar Romeny, J. Koenderink, and M. Viergever, Cartesian differential invariants in scale-space, *J. Math. Imaging Vision* **3**, 1993, 327–348.
15. L. Florack, B. ter Haar Romeny, J. Koenderink, and M. Viergever, General intensity transformations and differential invariants, *J. Math. Imaging Vision* **4**, 1994, 171–187.
16. T. Freeman, Calculating catchment area with divergent flow based on a regular grid, *Comput. Geosci.* **17**, 1991, 413–422.
17. J. Gauch and S. Pizer, Multiresolution analysis of ridges and valleys in grey-scale images, *IEEE Trans. Pattern Anal. Machine Intelligence* **15**, 1993, 635–646.
18. L. J. Gibson, Mechanical behavior of cancellous bone, *J. Biomechanics* **18**(5), 1985, 317–328.
19. L. Griffin and A. Colchester, Superficial and deep structure in linear diffusion scale space: Isophotes, critical points and separatrices, *Image Vision Comput.* **13**, 1995, 543–557.
20. L. Griffin, A. Colchester, and G. Robinson, Scale and segmentation of grey-level images using maximum gradient paths, *Image Vision Comput.* **10**, 1992, 389–402.
21. R. Haralick, Ridges and valleys on digital images, *Comput. Vision Graphics Image Process.* **22**, 1983, 28–38.
22. B. Jähne, *Spatio-Temporal Image Processing*, Vol. 751 of Lecture Notes in Computer Science, Chap. 8, pp. 143–152, Springer-Verlag, Berlin/New York, 1993.
23. A. Jain, L. Hong, and R. Bolle, On-line fingerprint verification, *IEEE Trans. Pattern Anal. Machine Intelligence* **19**, 1997, 302–313.
24. J. Koenderink and A. van Doorn, Local features of smooth shapes: Ridges and courses, in *Geometric Methods in Computer Vision II*, Vol. 2031, pp. 2–13, SPIE, Bellingham, WA, 1993.
25. I. Kweon and T. Kanade, Extracting topographic terrain features from elevation maps, *CVGIP Image Understanding* **59**, 1994, 171–182.
26. S. Lee and Y. Joon, Direct extraction of features for gray scale character recognition, *IEEE Trans. Pattern Anal. Machine Intelligence* **17**, 1995, 724–729.
27. M. Leyton, Symmetry-curvature duality, *Comput. Vision Graphics Image Process.* **38**, 1987, 327–341.
28. R. Lindsay, Prevention and treatment of osteoporosis, *Lancet* **341**, 1993, 801–805.
29. D. Lloret, A. López, J. Serrat, and J. Villanueva, Creaseness-based CT and MR registration: Comparison with the mutual information method, *J. Electronic Imaging* **8**, 1999, 255–262.
30. A. López, Ph.D. thesis, Universitat Autònoma de Barcelona, Spain, 1999.
31. A. López, F. Lumbreras, J. Serrat, and J. Villanueva, Evaluation of methods for ridge and valley detection, *IEEE Trans. Pattern Anal. Machine Intelligence* **21**, 1999, 327–335.
32. A. López, W. Niessen, J. Serrat, K. Nicolay, B. ter Haar Romeny, J. Villanueva, and M. Viergever, New improvements in the multiscale analysis of trabecular bone patterns, in *8th Spanish National Symposium on Pattern Recognition and Image Analysis* (A. Sanfeliu and M. Torres, Eds.), Vol. 1, pp. 497–504, 1999.
33. J. Maintz, P. van den Elsen, and M. Viergever, Evaluation of ridge seeking operators for multimodality medical image matching, *IEEE Trans. Pattern Anal. Machine Intelligence* **18**, 1996, 353–365.
34. D. Maio and D. Maltoni, Direct gray-scale minutiae detection in fingerprints, *IEEE Trans. Pattern Anal. Machine Intelligence* **19**, 1997, 27–39.
35. D. Mark, Automated detection of drainage networks from digital elevation models, *Cartographica* **21**, 1984, 168–178.

36. J. Maxwell, On hills and dales, *London, Edinburgh Dublin Philos. Mag. J. Sci.* **40**, 1870, 421–425.
37. O. Monga and S. Benayoun, Using partial derivatives of 3D images to extract typical surface features, *CVGIP Image Understanding* **61**, 1995, 171–189.
38. B. Morse, S. Pizer, and A. Liu, Multiscale medial analysis of medical images, in *Information Processing in Medical Imaging* (Barrett and Gmitro, Eds.), Vol. 687 of LNCS, pp. 112–131, Springer-Verlag, Berlin/New York, 1993.
39. L. Nackman, Two-dimensional critical point configuration graphs, *IEEE Trans. Pattern Anal. Machine Intelligence* **6**, 1984, 442–450.
40. L. Najman and M. Schmitt, Watersheds of a continuous function, *Signal Process.* **38**, 1994, 99–112.
41. W. Niessen, Ph.D. thesis, Utrecht University, The Netherlands, 1997.
42. W. Niessen, A. López, W. Van Enk, P. Van Roermund, B. ter Haar Romeny, and M. Viergever, In vivo analysis of trabecular bone architecture, in *Information Processing and Medical Imaging* (J. S. Duncan and G. Gindi, Eds.), Vol. 1230 of Lecture Notes in Computer Science, pp. 435–440, 1997.
43. W. Niessen, A. López, W. Van Enk, P. Van Roermund, B. ter Haar Romeny, and M. Viergever, Multiscale trabecular bone orientation analysis, in *7th Spanish National Symposium on Pattern Recognition and Image Analysis* (A. Sanfeliu, J. Villanueva, and J. Vitrià, Eds.), Vol. 1, pp. 19–24, Centre de Visió per Computador, Universitat Autònoma de Barcelona, 1997.
44. J. O’Callaghan and D. Mark, The extraction of drainage networks from digital elevation data, *Comput. Vision Graphics Image Process.* **28**, 1984, 323–344.
45. S. Pizer, C. Burbeck, J. Coggins, D. Fritsch, and B. Morse, Object shape before boundary shape: Scale–space medial axes, *J. Math. Imaging Vision* **4**, 1994, 303–313.
46. W. Press, S. Teukolsky, W. Vetterling, and B. Flannery, *Numerical Recipes in C*, 2nd ed., Cambridge Univ. Press, Cambridge, UK, 1992.
47. P. Rosin, Early image representation by slope districts, *J. Visual Comm. Image Represent.* **6**, 1995, 228–243.
48. H. M. Schey, *DIV, GRAD, CURL and all that*, Norton, New York, 1973.
49. W. Seemuller, The extraction of ordered vector drainage networks from elevation data, *Comput. Vision Graphics Image Process.* **47**, 1989, 45–58.
50. P. J. Soille and C. Gratin, An efficient algorithm for drainage network extraction on DEMs, *J. Visual Comm. Image Represent.* **5**, 1994, 181–189.
51. C. Studholme, D. Hill, and D. Hawkes, Automated 3D registration of MR and CT images of the head, *Med. Image Anal.* **1**, 1996, 163–175.
52. B. ter Haar Romeny and L. Florack, A multiscale geometric model of human vision, in *The Perception of Visual Information* (W. Hendee and P. Well, Eds.), pp. 73–114, Springer-Verlag, Berlin/New York, 1993.
53. J. P. Thirion and A. Gourdon, Computing the differential characteristics of iso-intensity surfaces, *CVGIP Image Understanding* **61**, 1995, 190–202.
54. L. Vincent and P. Soille, Watersheds in digital spaces: An efficient algorithm based on immersion simulations, *IEEE Trans. Pattern Anal. Machine Intelligence*, **13**, 1991, 583–598.
55. L. Wang and T. Pavlidis, Direct gray-scale extraction of features for character recognition, *IEEE Trans. Pattern Anal. Machine Intelligence* **15**, 1993, 1053–1067.
56. W. Wells, P. Viola, and R. Kikinis, Multi-modal volume registration by maximization of mutual information, in *Medical Robotics and Computed Assisted Surgery*, pp. 55–62, Wiley-Liss, New York, 1995.
57. J. West, J. Fitzpatrick, M. Wang, B. Dawant, C. Maurer, R. Kessler, R. Maciunas, C. Barillot, D. Lemoine, A. Collignon, F. Maes, P. Suetens, D. Vandermeulen, P. van den Elsen, S. Napel, T. Sumanaweera, B. Harkness, P. Hemler, D. Hill, D. Hawkes, C. Studholme, J. Maintz, M. Viergever, G. Malandain, X. Pennec, M. Noz, G. Maguire, M. Pollack, C. Pelizzari, R. Robb, D. Hanson, and R. Woods, Comparison and evaluation of retrospective intermodality brain image registration techniques, *J. Comput. Assisted Tomography* **21**, 1997, 554–556.
58. A. Yuille and M. Leyton, 3D symmetry-curvature duality theorems, *Comput. Vision Graphics Image Process.* **52**, 1990, 124–140.